

# Disease-Associated Mutations in Tau Encode for Changes in Aggregate Structure Conformation

Kerry T. Sun, Tark Patel, Sang-Gyun Kang, Allan Yarahmady, Mahalashmi Srinivasan, Olivier Julien, Jónathan Heras, and Sue-Ann Mok\*



Cite This: *ACS Chem. Neurosci.* 2023, 14, 4282–4297



Read Online

ACCESS |



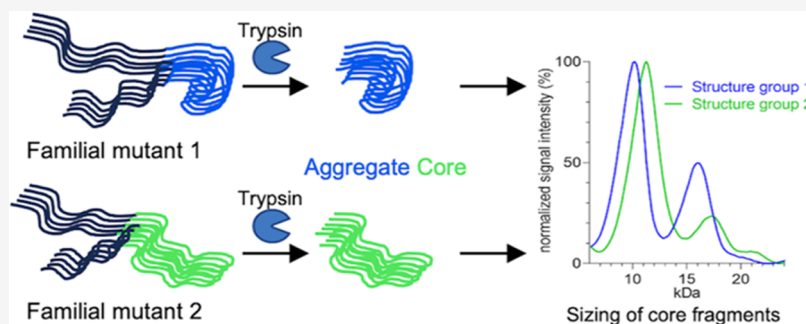
Metrics & More



Article Recommendations



Supporting Information



**ABSTRACT:** The accumulation of tau fibrils is associated with neurodegenerative diseases, which are collectively termed tauopathies. Cryo-EM studies have shown that the packed fibril core of tau adopts distinct structures in different tauopathies, such as Alzheimer's disease, corticobasal degeneration, and progressive supranuclear palsy. A subset of tauopathies are linked to missense mutations in the tau protein, but it is not clear whether these mutations impact the structure of tau fibrils. To answer this question, we developed a high-throughput protein purification platform and purified a panel of 37 tau variants using the full-length 0N4R splice isoform. Each of these variants was used to create fibrils *in vitro*, and their relative structures were studied using a high-throughput protease sensitivity platform. We find that a subset of the disease-associated mutations form fibrils that resemble wild-type tau, while others are strikingly different. The impact of mutations on tau structure was not clearly associated with either the location of the mutation or the relative kinetics of fibril assembly, suggesting that tau mutations alter the packed core structures through a complex molecular mechanism. Together, these studies show that single-point mutations can impact the assembly of tau into fibrils, providing insight into its association with pathology and disease.

**KEYWORDS:** tau aggregation, tauopathies, disease mutations, aggregation kinetics, protein conformation, proteolysis

## INTRODUCTION

Tauopathies are a group of neurodegenerative disorders that feature the pathological accumulation of aggregates containing microtubule-associated protein tau.<sup>1,2</sup> The fibrillar forms of tau aggregates are characteristically composed of a core region containing regularly tightly packed monomer sequences rich in  $\beta$ -sheet structure that are surrounded by more loosely packed or disordered N- and C-terminal sequences termed the “fuzzy coat”.<sup>3–5</sup> Protease digestion of tau fibrils isolated from patient samples defined the sequences protected within the tightly packed core and suggested that (1) tau can adopt multiple conformations in fibril structures and (2) specific fibril structures tracked with individual tauopathies: Alzheimer's disease (AD), Pick's disease (PD), corticobasal degeneration (CBD), and progressive supranuclear palsy (PSP).<sup>6–15</sup> The distinct features of tau fibril core structures from multiple tauopathies have now been confirmed to atomic resolution by Cryo-electron microscopy (Cryo-EM).<sup>10–15</sup> Prion-like properties have been ascribed to tau<sup>16,17</sup> in which the conformation

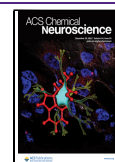
of the tau aggregate promotes aggregate propagation via cell-to-cell spreading and faithful recruitment and templating of its structure to native tau monomers.<sup>18–21</sup> Tau aggregates isolated from tauopathies and introduced to cells display differential requirements for templating aggregation,<sup>22</sup> and when AD, CBD, or PSP fibrils are injected into mice, they promote distinct patterns of pathology that share qualities with the corresponding human disease.<sup>23</sup> Thus, understanding the mechanisms by which distinct tau aggregate structures are generated and how they are linked to tauopathies would

**Received:** June 17, 2023

**Revised:** November 16, 2023

**Accepted:** November 17, 2023

**Published:** December 6, 2023



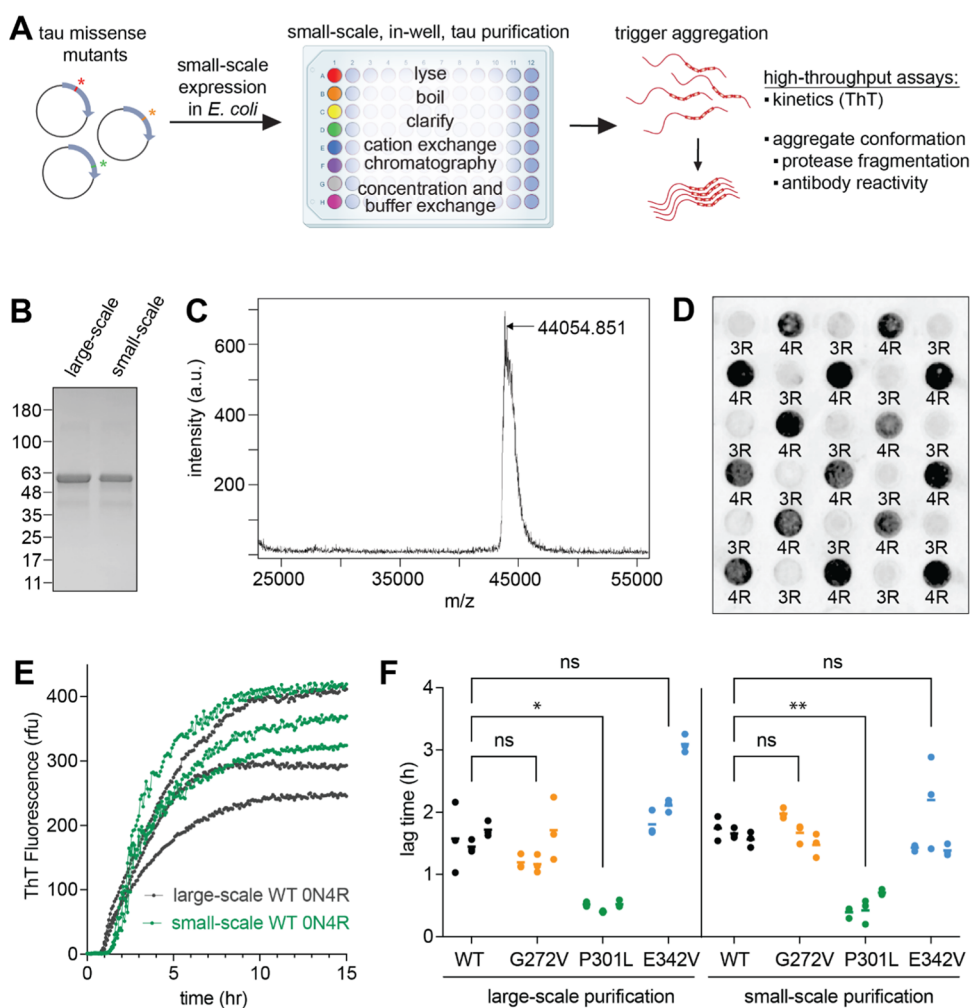


**Figure 1.** Validation of high-throughput, small-scale purification and aggregation platform for recombinant tau. (A) Major components of the tau purification and downstream assay platform. Tau constructs with encoded disease-associated mutations are expressed in small-volume *E. coli* cultures and then lysed and purified in 96-well plates. (B) SDS-PAGE comparison of purified WT 0N4R tau using a large-scale protocol or our small-optimized scale protocol. The MW of tau is 44 kDa; however, the protein migrates at an apparent MW of ~50 kDa due to a high number of positively charged residues. Results representative of 3 independent protein preparations. (C) Mass spectrum of small-scale purified tau demonstrating a single peak corresponding to the calculated mass of the full-length protein. Results representative of 3 independent protein preparations. (D) Dot blot demonstrating no cross-contamination of tau samples during small-scale purification. Cultures overexpressing 0N4R or 0N3R WT tau were purified in alternating wells of a 96-well plate. Purified proteins were transferred to dot blot while maintaining their relative plate position: 4R = 0N4R, 3R = 0N3R. The blot was probed with a 4R tau antibody (ET3) recognizing an epitope found in 4R but not 3R tau isoforms. (E) Aggregation kinetic curves for WT 0N4R tau purified using large-scale versus small-scale methods. Aggregation reactions were initiated by introducing heparin to 10  $\mu$ M tau, and the reaction was monitored with ThT. The individual curves for three technical replicates are plotted. (F) Comparison of lag time values for WT 0N4R tau and mutants (G272V, P301L, E342V) purified via large- or small-scale protocols. For each tau variant, individual lag time values for three technical replicates (aligned dots), assayed from three individual protein preparations (side-by-side columns of dots) are plotted along with the mean for each experiment (bar). \* $p < 0.05$ , \*\* $p < 0.01$ , nested one-way analysis of variance (ANOVA), post hoc Dunnett's test.

contribute to a better molecular understanding of the genesis and progression of these diseases.

Over 50 mutations in the *MAPT* gene that encodes tau have been linked to tauopathies.<sup>24</sup> The collection of mutations show heterogeneity with respect to penetrance, age of onset, clinical phenotypes, and their association with individual tauopathies.<sup>24–29</sup> At the molecular level, individual tau mutations have also been shown to differentially modulate tau biochemical properties, and cellular dysfunction associated with pathogenesis. For example, intronic mutations (and some missense mutations) alter the regulation of tau splicing and the resulting composition of tau isoforms expressed.<sup>30–32</sup> Individual missense mutations have been shown to differ from wild-

type (WT) in one or more properties including aggregation propensity,<sup>33–35</sup> cellular aggregate seeding,<sup>36,37</sup> microtubule binding and dynamics,<sup>35,38–41</sup> protein interaction partners,<sup>42,43</sup> post-translational modifications,<sup>44,45</sup> engagement and processing by the protein quality control machinery,<sup>43,46–48</sup> and axonal functions.<sup>49,50</sup> Mice expressing individual tau missense mutants produce distinct phenotypic profiles in regard to cellular dysfunction, patterns and timing of tau aggregate pathology, and behavioral deficits.<sup>51</sup> In light of the evidence of multiple tau aggregate conformations linked to tauopathies, we reasoned that one potential factor that could contribute to the pathogenic effects of tau mutations is their ability to promote

the formation of alternate tau aggregates, which have not been extensively investigated.

Although there have been previous studies of structural differences induced by a small subset of mutations in short synthetic constructs of tau,<sup>52,53</sup> comparison of the effects of a broad set of tau mutations in the context of full-length tau has not been characterized. One of the hurdles to this goal is the development of high-throughput methods for the production of tau variants and comparisons of their relative structures. To address this issue, we developed a high-throughput approach for the expression and plate-based purification of recombinant tau mutant proteins. This advancement allowed us to generate a panel of 37 tau variants (WT + 36 missense mutants). Using low-volume, high-throughput thioflavin T (ThT) and trypsin digestion assays, we profiled the rate and extent of aggregation *in vitro* and the effects of the mutations on the proteolytic sensitivity of the resulting fibril core regions. This approach enabled us to perform a cross-comparison of structural profiles with properties such as aggregation kinetics. Strikingly, we found that a subset of missense mutations was sufficient to alter the proteolytic sensitivity of tau fibrils when compared to WT, which may partially explain their link to disease. More broadly, we suggest that this experimental platform can be used and adapted to systematically understand the complex relationships between tau sequence, aggregation propensity, fibril structure, and cellular dysfunction.

## RESULTS AND DISCUSSION

**Validate a High-Throughput Tau Purification Platform.** Our first objective was to be able to directly compare our 37 disease-associated tau mutants with respect to multiple aggregation properties. Tau transcripts are subject to alternative splicing, leading to the production of multiple tau isoforms. Six major tau isoforms are prevalent in the adult central nervous system (CNS) and differ in the inclusion/exclusion of two N-terminal inserts (0N, 1N, or 2N) and three versus four microtubule binding repeats (3R, 4R). For our study, we targeted the introduction of familial mutations into the 0N4R tau isoform because it is a major component of tau aggregates in multiple tauopathies (AD, PSP, CBD)<sup>54,55</sup> and it aggregates relatively rapidly *in vitro*.<sup>46</sup> We developed a platform for purifying recombinant human 0N4R tau protein in a 96-well plate format (Figure 1A) so that all individual tau mutants could be purified in parallel and the entire mutant panel could be assayed across multiple protein preparations. Our small-scale tau purification protocol retained the major procedures reported in traditional large-scale methods including protein expression in *Escherichia coli*, boiling of the lysate, cation exchange and buffer exchange into standard conditions (D-PBS, 2mM DTT, pH 7.4) suitable for protein aggregation assays.<sup>33,46,56</sup> Sodium dodecyl sulfate polyacrylamide gel electrophoresis (SDS-PAGE) of small-scale purified WT 0N4R tau migrated as the expected full-length form, similar to the same tau construct obtained from a traditional large-scale purification protocol (Figure 1B). Matrix-assisted laser desorption/ionization time-of-flight (MALDI-TOF) analysis of small-scale purified 0N4R WT tau detected a single major species at 44054 *m/z*, closely corresponding to the predicted full-length product (Figure 1C). To test the potential for cross-contamination of proteins between individual wells, we purified two different isoforms of tau (0N3R and 0N4R) arranged in alternating wells within the plate (Figure 1D). The purified samples were subjected to a dot blot with an antibody

specifically recognizing the 0N4R isoform. Antibody reactivity was only detected in the purified 0N4R samples and not the 0N3R sample purified from adjacent wells suggesting minimal/no cross-contamination occurs between wells during purification. Each in-well purification yielded on average >200  $\mu\text{g}$  of purified tau prepped for downstream assays (Figure S1A).

Individual disease-associated mutations were introduced into human 0N4R tau by site-directed mutagenesis and purified by using our small-scale purification platform. SDS-PAGE analysis of the mutant constructs isolated by the small-scale method demonstrated consistent purities across the entire panel (Figure S2). We then compared large- and small-scale purified tau in an *in vitro* aggregation assay for a subset of tau mutants (WT, G272V, P301L, E342V). Each tau mutant was assayed across three different protein preparations for each purification method. Assays were carried out in miniaturized 384-well format aggregation kinetic assays that we previously developed,<sup>46</sup> which requires less than 9  $\mu\text{g}$  of tau protein per reaction. Tau aggregation was tracked with the fluorescent amyloid dye Thioflavin T (ThT) following the addition of a common aggregation accelerant, heparin. An example of the kinetic aggregation curves obtained for large-scale versus small-scale purified WT 0N4R tau is shown in Figure 1E.

Individual aggregation curves were fitted to the Gompertz function for comparative analyses of the shape of the curves with respect to three parameters: lag time, amyloid formation rate constant, and amplitude. Lag time represents the initial phase of aggregation, where the threshold conditions for rapid amyloid accumulation have not been met. The amyloid formation rate constant describes the net growth rate of amyloid fibrils in the reaction. The amplitude parameter describes the plateau value reached following the rapid amyloid formation phase. Between tau mutants tested, similar relationships were observed with respect to the extracted kinetic parameters (Figures 1F, S1B,C). For example, G272V tau consistently aggregated with a lag time similar to that of WT, whereas P301L tau had a significantly shorter lag time than that of WT (Figure 1F). Intrinsic variabilities in these calculated kinetic parameters were similar between protein samples from large-scale and small-scale purifications. Overall, these results support that tau purified using small-scale methods is comparable to tau purified by classical large-scale methods and critically, allows us to perform cross-comparisons of tau mutants for their aggregation properties at a higher-throughput capacity.

**Tau Disease-Associated Mutations Drive the Formation of Aggregate Structures Distinct from WT.** We next determined whether single tau mutations were sufficient to promote the formation of alternative aggregate structures. As a readout of aggregate structure, we used protease digestion of aggregated tau to identify tau fragments buried in the tightly packed aggregate core that are more protected from protease activity. The specific pattern of protected tau fragments has been used to detect distinct aggregate species in both recombinant tau and disease patient samples.<sup>6,7,21</sup> We first explored the kinetics of digestion for WT 0N4R tau with the protease, trypsin. The tau protein contains trypsin sites spread throughout its sequence at an average of one site every 8 residues making it a robust sensor of changes in tau sequence accessibility/structure (Figure S3A). WT 0N4R tau was incubated with heparin and allowed to aggregate for 24 h prior to direct digestion of the reaction with mass spectrometry grade trypsin (has enhanced stability and no chymotrypsin

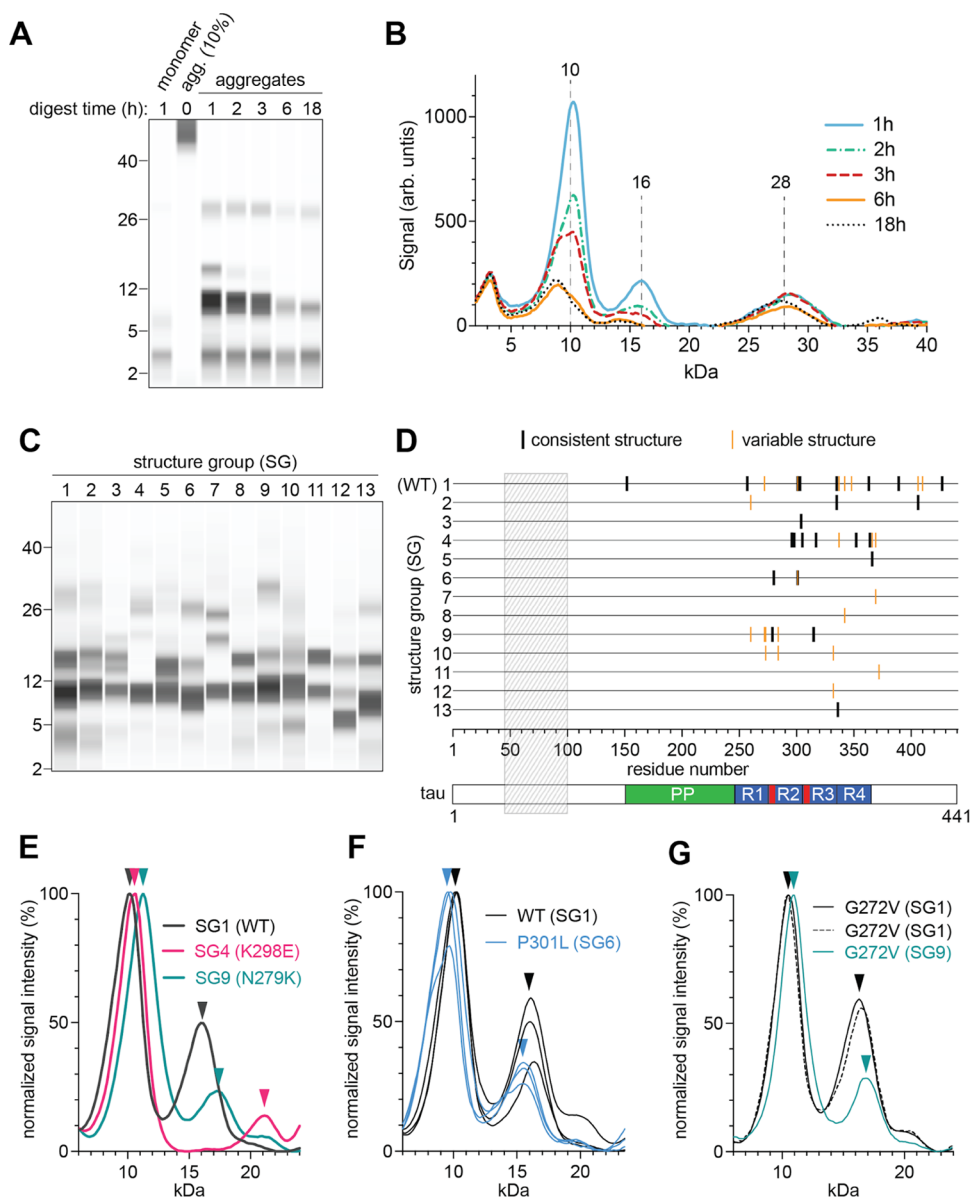


**Figure 2.** Tau mutations promote aggregate structures distinct from WT as shown by altered trypsin digestion fragment profiles. (A, B) Time course of trypsin digestion of WT 0N4R tau aggregates. Samples were processed for capillary gel electrophoresis and total protein detection (lysine-dependent labeling) of protease-resistant fragments. Trypsin is not detected due to lysine modification of the protease. Results represent three independent experiments. (A) Capillary lane view of trypsin-resistant fragments following digestion with trypsin for indicated times. Migration of MW standards (kDa) marked (left). (B) Corresponding chromatograms from (A) for trypsin-digested aggregate samples. Major peaks are marked by vertical dashed lines with MW. (C) Lane view of representative digest profiles for SGs 1–13. Migration of MW standards (kDa) marked (left). (D) 0N4R tau mutants plotted according to their location within the tau sequence (*x*-axis) and SG classification (*y*-axis). Numbering for *x*-axis corresponds to 2N4R tau isoform. A schematic of tau with major sequence regions labeled is shown below graph: PP = polyproline region, R1–R4 = microtubule binding repeat regions, red boxes = aggregation motif locations. Hatched box marks sequence region not included in the 0N4R tau isoform. Tau mutants that gave an alternate profile in at least one experiment were classified as having variable structure (orange lines, all SG marked for each mutant). (E–G) Chromatograms of fragment profiles for indicated tau mutants over the 6–24 kDa region. For the *y*-axis, signal intensity is normalized with the maximal signal value set to 100%. Each profile is colored according to mutant/SG. Matching colored arrowheads mark the maxima of major peaks. (E) Representative fragment profiles of three major structure groups defined in this study: SG1, SG4, and SG9. (F) Replicate fragment profiles for WT 0N4R tau and P301L 0N4R tau ( $n = 3$  independent experiments). (G) Replicate fragment profiles for the variable structure mutant, G272V 0N4R tau ( $n = 3$  independent experiments).

activity) for 0, 1, 2, 3, 6, and 18 h. Capillary gel electrophoresis combined with total protein detection was used to quantify the migration and relative amounts of trypsin-resistant fragments. The technique is highly sensitive and can detect the fragments produced from as little as 0.8  $\mu\text{g}$  of a digested tau aggregate sample. Figure 2A displays the simulated lane view of the fragments for individual samples, and Figure 2B shows the

chromatogram profiles of the corresponding samples. Serendipitously, trypsin itself is not detected in our profiles since the mass spectrometry grade trypsin is modified at lysine residues utilized by the total protein detection method. Monomer tau treated with trypsin was completely digested to 2–3 kDa fragments within 1 h of trypsin treatment. Undigested tau aggregates migrated at >40 kDa corresponding to the expected

Table 1. Structure Group Classifications of Tau Mutants Based on their Trypsin-Resistant Fragment Profiles

		Structure group														
		1	2	3	4	5	6	7	8	9	10	11	12	13		
Tau mutants (ordered by relative position in primary sequence)	WT															
	A152T															PP
	K257T															R1
	I260V									I260V						
	G272V									G272V						
											G273R	G273R				R2
											N279K					
											ΔK280					
											L284R	L284R				
																R3
																R4
																C-terminal region

<sup>a</sup>Individual tau mutants are binned into SGs 1–13 (columns). Mutants in the table are ordered in rows based on their relative sequence location. Mutants with a consistent SG across all independent experiments ( $n = 3$ ) are colored in black. Mutants binned into more than one SG are colored red (2 experiments) and orange (1 experiment). The tau sequence region associated with each mutant is indicated at the far right-hand column of the table: PP = polyproline; R1–R4 = microtubule binding repeat regions 1–4.

size of full-length tau. Loss of full-length tau after trypsin addition coincided with the generation of smaller peptide fragments. At 1 and 2 h digest time points, the pattern of produced fragments was fairly consistent giving three major fragment peaks at 10, 16, and 28 kDa and confirmed the presence of a stable core that is relatively refractory to trypsin digestion of its internal sequences. Similar to the digested monomer tau control sample, a major peak at 2 kDa was also observed. Since our aggregated samples were not further purified prior to trypsin treatment, the 2 kDa band likely corresponds to unaggregated tau present within our original reactions. At 3, 6, and 18 h time points, a shift of 1–2 kDa toward smaller MWs was observed for each of the major fragments. For example, at the 3 h digest time point, a 9 kDa band was detected along with the 10 kDa band. By 6 h, only the 9 kDa band was the major peak. These results likely suggest prolonged trypsin treatment leads to increased digestion from the core fragment ends. Based on these results, digestion reactions were kept to <2 h for the remainder of the study. Using our digest conditions, we directly compared the protease-resistant fragment profiles for aggregates generated from WT tau and 36 disease-associated tau mutants. Tau variants were small-scale purified in parallel, aggregated, and trypsin-digested with the same reaction conditions. We observed that a subset of tau mutants produced a digest fragment profile that differed from WT tau. To systematically compare the trypsin digest fragment profiles of individual samples and identify distinct profiles, we developed an algorithm to process gel chromatogram data and perform hierarchical cluster analysis (see the [Methods](#) section for details). Clustering is based on the similarity of the overall shape of the chromatogram profile (relative peak heights and distances). We restricted analysis to the 6–24 kDa range which we observed more consistently detected signals from fragments above background levels. We applied the analysis to a data set containing three independent digest reactions for each tau variant within our panel. Using a 90% threshold for similarity, the data set was binned into 13 separate profiles ([Figure S4](#)) that we term “structure groups” (SG). The representative fragment profile for each structure group is presented in [Figure 2C](#). The profile for WT tau corresponds to the pattern for structure group 1 (SG1) and the remaining structure groups are ordered as a function of decreasing similarity score relative to SG1. [Figure 2D](#) shows a schematic of the distribution of tau mutants in each structure group and their relative locations within the tau sequence. In the corresponding table ([Table 1](#)), the structure group(s) of each tau mutant are indicated.

Within the panel, the majority of tau mutants binned into 3 major structure groups: SG1, SG4, and SG9. Collectively, these groups matched at least one replicate for 80% (29/36) of the tau mutant digest profiles. Representative profiles comparing SG1, SG4, and SG9 are shown in [Figure 2E](#). SG1 which represents the fragment profile for WT tau was the largest grouping of mutants (15/36) and included 10 tau mutants that invariably shared this profile (e.g., A152T, P301S, G335V) and another 5 mutants that generated the profile in at least 1 of 3 independent assays (e.g., G272V, V337M, R406W). The tau mutants belonging to SG1 were spread across the tau sequence, showing no clustering to a specific sequence region. Tau mutants in SG4 (10/36) also did not show any association

with a specific location. SG4 contained relatively rare FTLD-tau mutations with the exception of V337M which could generate more than one structure profile (SG1 and SG4). SG9 contained 6 mutants (I260V, G272V, G273R, N279K, L284R, L315R) that did seem to cluster in the first two microtubule binding repeat regions of tau (R1–R2); however, one of the mutants, L315R, was located further downstream in R3. Strikingly, there was little to no overlap between the profiles generated for the tau variants within SG1, SG4, and SG9; V337M was the only mutant shared between major structure groups (SG1 and SG4). With respect to the other structure groups, some contained just a single mutant (G304S, G366R, K369I, P332S, Q336R, E342V, E372G), whereas other groups contained up to 3 mutants. The core packing of aggregates for the vast majority of the mutants we tested has not been previously characterized. However, Aoyagi et al. have compared the packing of WT, P301L, and R406W ON4R tau via pronase treatment.<sup>57</sup> They found that the P301L mutation produced aggregates with a digest fragment profile distinct from that of WT tau. We also found that P301L tau consistently classified into a different structure group (SG6) than WT ([Figure 2F](#)). The Aoyagi study<sup>57</sup> also reported that WT and R406W tau aggregates shared a similar digest fragment profile. In contrast, we detected that R406W tau aggregate structures could be matched to the WT in only two out of three of our trials. For one R406W tau aggregate reaction, we detected a packed core that was distinct from WT. All of the aggregates formed by tau mutants in the panel were confirmed to be positive for ThT binding in our aggregation kinetic assays, indicating that they contain  $\beta$ -sheet-rich properties characteristic of amyloids. Thus, our data set highlights the diversity of amyloid structures formed by these disease-associated mutations and offers evidence of how their pathological misfolding can be readily differentiated from that of WT tau.

One key observation that emerged from our large mutant panel analysis was that a subset of mutants such as V337M generated more than one digest fragment profile between experiments, which we termed “variable structure” mutants. Within our panel, 30% (11/36) of the tau mutants assayed had variable structure and are highlighted in [Table 1](#) (red and orange) and in [Figure 2D](#) (orange). These variable structure mutants, in general, displayed one structure profile that fell into the major structure groups (SG1, SG4, or SG9) and another alternate structure profile. An example of the digest profiles generated by the variable tau mutant G272V is shown in [Figure 2G](#). The alternate structure could group with other mutant profiles (e.g., P301T, deltaK280, and P301L group in SG6) or could be classified as a unique structure in some cases (e.g., G366R = SG5, K369I = SG7, E342V = SG8). Since we did not detect variable structures for WT and the majority of tau mutants, it suggests that there is a predominant misfolding pathway for most tau variants but that some mutations allow for the occurrence of an early aggregate species or event that can shuttle tau down an alternative divergent misfolding pathway(s).

Even with the large panel of mutants analyzed, no clear relationships could be identified between the biochemical changes in tau caused by mutation and their classification into specific structural groups. No overall trend was observed

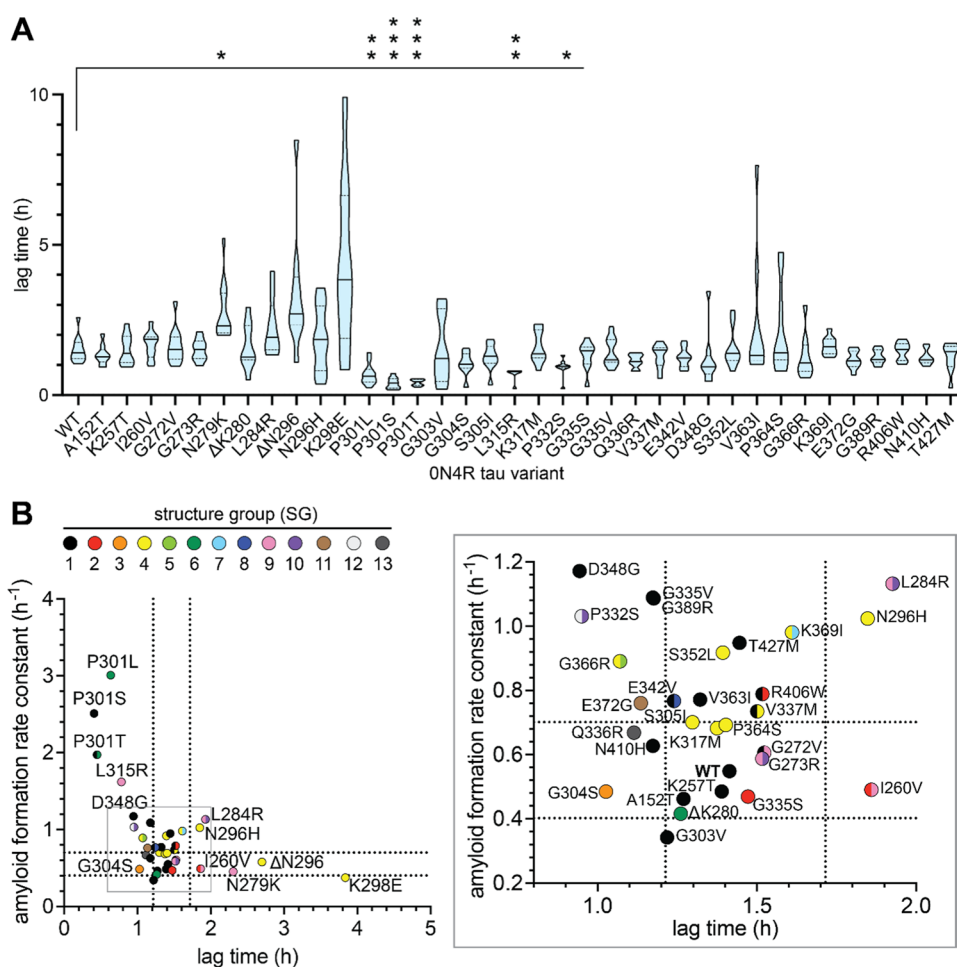


**Figure 3.** Mutation-dependent alterations in tau aggregation kinetics do not predict changes in aggregate structures. (A) Lag time of individual tau WT and mutants. The median (solid line) and quartiles (dotted lines) are plotted for each variant ( $n \geq 9$  replicates,  $\geq 3$  independent experiments). Brown-Forsythe and Welch ANOVA was performed with post hoc comparisons to the WT tau group.  $p = * < 0.05$ ,  $** < 0.01$ ,  $*** < 0.0001$ . (B) Comparison of WT and tau mutants with respect to amyloid formation rate constant, lag time, and structure group classification. For each tau variant, median lag time and amyloid formation rate constant values are plotted ( $n \geq 9$  replicates,  $\geq 3$  independent experiments) and circles filled by determined SG(s) as designated in the legend. Variable structure tau mutant data points are colored with corresponding SG as half-circles. The quartile boundaries of lag time and amyloid formation rate constant values for WT tau are marked by dashed lines. Graph showing all assayed tau variants (left) with gray boxed region expanded to aid in comparison of mutants clustered in this region (right).

between the relative locations of the mutations and their grouping in a structure group. The strongest trend was observed for SG9 that contained several mutations clustered between residues 260–284 but mutations within this sequence (deltaK280) did not generate the same structure, and mutations outside the 260–284 region could also generate the SG9 fragment profile (L315R). We found no correlations between changes in the protein's isoelectric point or hydrophobicity values and structure group classifications (Figure S3B,C). We also observed that varying the missense mutation at the same residue (e.g., G335 and P301) could give rise to alternate structure groups. G335V gave a digest profile matching WT tau, whereas G335S gave rise to an alternate digest profile (SG2). At the P301 residue, mutation to a leucine (P301L) generated aggregates classed into SG6 (Figure 2F), whereas mutation to a serine (P301S) gave rise to aggregates similar to WT (SG1). Interestingly, the P301T mutation fell into the variable structure category and could form both the SG1 and SG6 structures. These results begin to reveal the complex nature of the effects of tau mutations on

aggregate structure formation, where even subtle differences at a given residue can significantly alter the reaction products.

### Aggregation Kinetics of Individual Tau Mutants Is Not a Predictor of Distinct Aggregation Structure Profiles.

We further probed whether the alterations in aggregate structure we detected could be linked to other tau properties, such as aggregation kinetics. We carried *in vitro* aggregation kinetic assays for the entire tau mutant panel (WT and 36 mutants). We found that the extracted kinetic parameters (lag time, amyloid formation rate constant, and amplitude) contained some variation when tested across multiple independent experiments and protein preparations, as expected (Figures 3A, S5A,B). For WT tau, absolute calculated lag times varied from 1.04 to 2.5 h (median = 1.41 h, quartiles = 1.21, 1.76). The largest variance in lag time was observed for K298E tau (median = 3.84 h, quartiles = 1.89, 6.64). We also noted that large variations in one kinetic parameter for a mutant did not correlate with variability in other kinetic parameters. For example, K298E showed relatively little variability in amyloid formation rate constant or amplitude values compared to most mutants. Within the

Table 2. Predicted Effect of Tau Disease-Associated Mutations on Tau Fibril Structures<sup>a</sup>

Tau mutation	Fibril source	Patient-derived fibrils				Recombinant tau fibrils		
	PDB ID	AD SF	AD PHF	CBD	PSP	snake	twister	jagged
	WT structure? (Y/N/Partial)	5O3T	6HRE	6TJO	7U0Z	6QJH	6QJM	6QJP
A152T	Y							
K257T	Y							
I260V	N							
G272V	Partial							
G273R	N							
N279K	N							
ΔK280	N							
L284R	N							
ΔN296	N							
N296H	N							
K298E	N							
P301L	N							
P301S	Y							
P301T	Partial							
G303V	Y							
G304S	N							
S305I	N							
L315R	N							
K317M	N							
P332S	N							
G335S	N							
G335V	Y							
Q336R	N							
V337M	Partial							
E342V	Partial							
D348G	Y							
S352L	N							
V363I	Y							
P364S	N							
G366R	N							
K369I	N							
E372G	N							
G389R	Y							
R406W	Partial							
N410H	Y							
T427M	Y							

<sup>a</sup>Using the trypsin digest fragment profiles, mutations binned into the same structure group as WT tau (SG1) versus mutations that bin into another group or only with WT in some trials are labeled as Y(yes), N(no), or Partial, respectively. Tau mutations were modeled into Cryo-EM resolved tau fibril structures indicated using PyMOL. For each Cryo-EM structure analyzed, cells are colored according to whether the mutations are predicted to cause a steric clash (blue) or not (white). Mutations not present in solved structures are colored as gray cells.

panel, the P301 mutants (P301L, P301S, P301T) showed the largest variation in amyloid formation rate constant values. There was partial agreement between the heparin-induced aggregation kinetic values we obtained and those reported in previous studies for tau mutants. For example, P301L, P301S, and P301T mutants had significantly decreased lag times compared to WT.<sup>33,46,58,59</sup> However, we were not able to confirm previous evidence that other tau mutations (G272V, N279K, V337M, R406W) in the context of full-length tau also drove faster aggregation in the presence of heparin<sup>33</sup> or contrasting slower initial aggregation kinetics reported for R406W.<sup>33,59</sup> In the case of N279 K tau, we observed a significantly longer lag time than WT. The reason for this discrepancy is unclear but aggregation kinetics can be modulated by variables such as buffer conditions<sup>60,61</sup> and the tau isoforms<sup>62</sup> examined which differed between our current study and previous studies. It is possible that the presence of

mutations in the context of other reaction conditions may differentially modulate the aggregation kinetics.

We next plotted the median values for lag time against the amyloid formation rate constant and structure group for all tau variants in the panel (Figure 3B). We did not observe any clear trends between lag time or amyloid formation rate constant and specific structure groups. For example, tau mutants that promoted the formation of an alternative aggregate structure to WT could still have WT-like aggregation kinetics. Groups of tau mutants that were categorized to have the same aggregate structure profile could have dissimilar aggregation kinetic values in the parameters assessed. We also did not detect a relationship between amplitude and structure groups (Figure S5C) or kinetic parameters and variable versus consistent structure mutants (Figure S5D). Thus, variable aggregation kinetics that we measured can not readily account for the propensity of individual tau mutants to form alternate aggregate structures. However, it is important to state that



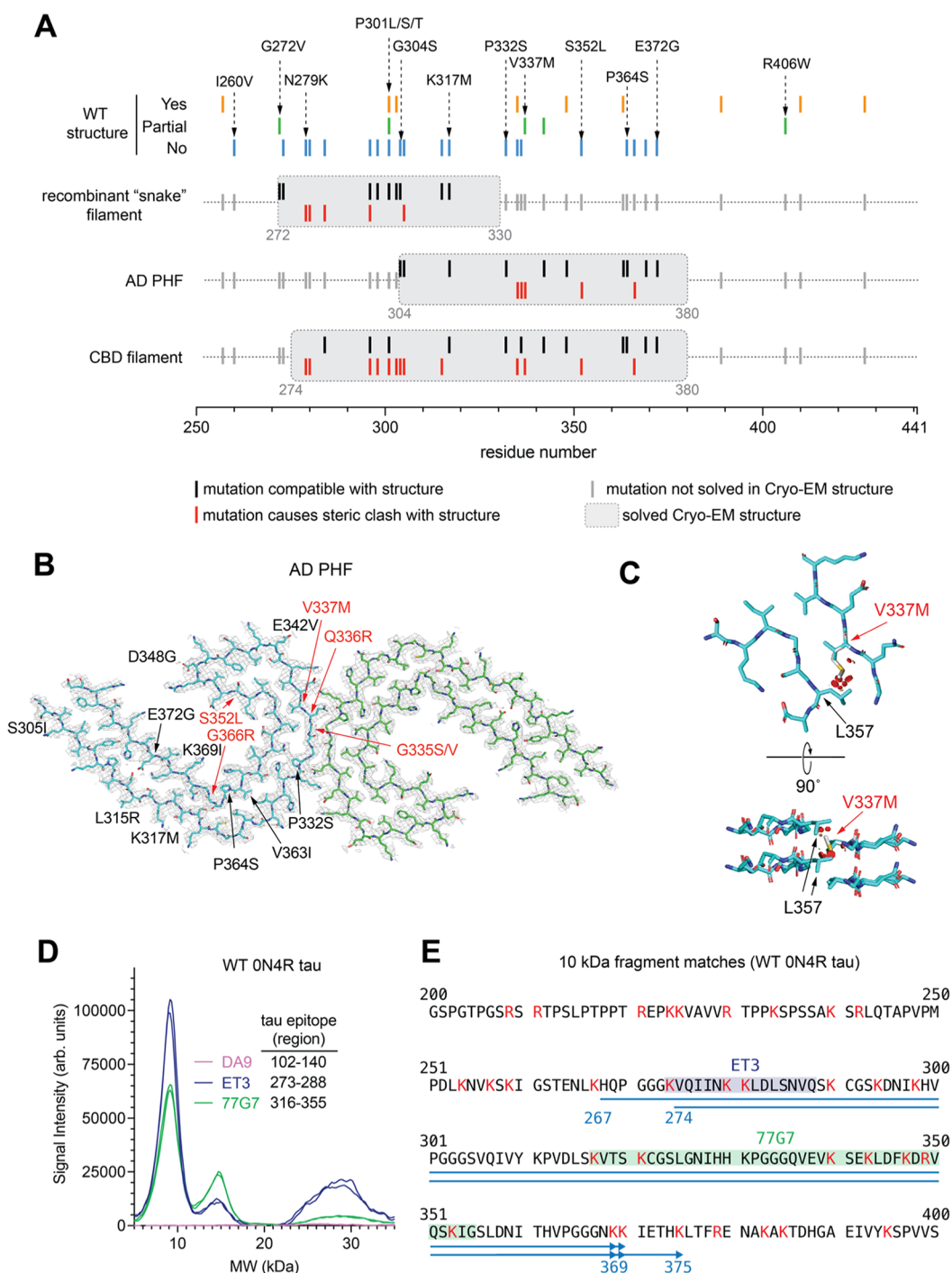


**Figure 4.** Predicted effects of disease-associated tau mutations in the context of Cryo-EM tau fibril structures. (A) Schematic displaying the location of tau mutations within sequence of indicated tau fibril structures solved by Cryo-EM. The schematic plus PDB file information for structures is summarized in Table 2. Top of the schematic indicates each mutation with respect to whether the determined SG matches with WT tau (lines: yes = orange, no = blue, and partial = green). For sequence regions included in Cryo-EM structures (gray box), individual mutation sites are colored according to whether they are predicted to cause a steric clash (red line) or not cause a steric clash (black line). Mutation sites not solved in structures are indicated as gray lines. (B) Cryo-EM density map (gray mesh) of AD PHF tau fibril (PDB: 6HRE). Individual protofibrils are shown as blue and green backbone traces. Disease-associated mutations assayed in our study are labeled on one protofibril (left) according to whether they are predicted to cause a steric clash (red) or not (black). (C) Residues surrounding residue V337 (blue backbone) in the same orientation as (B) or rotated 90°. The V337M mutation is superimposed onto the structure (white backbone), with predicted steric clashes with L357 indicated by red disks. (D, E) Epitope mapping of 10 kDa trypsin-resistant fragment for WT 0N4R tau. (D) Chromatogram of capillary electrophoresis immunoassay probed with tau antibodies DA9, ET3, and 77G7. (E) Tau amino acid sequence for residues 200–400 with predicted 10 kDa fragment identity underlined in blue (arrow = potential C-terminal ends). The epitope regions of ET3 (blue) and 77G7 (green) antibodies are highlighted. Lysine and arginine residues at predicted trypsin cleavage sites are colored in red.

aggregation of tau, similar to other amyloidogenic proteins, is a complex reaction where multiple types of molecular level processes are occurring in parallel such as primary nucleation, elongation, fragmentation, and secondary nucleation.<sup>58</sup> A limitation of our ThT kinetic assay methods is that they capture only the net contribution of these processes in the production of amyloid fibrils. It is possible that there is a significant correlation between the formation of specific tau aggregate conformations and aggregation subprocesses (e.g. fragmentation, elongation) that could be identified with methodologies capable of measuring these specific events.<sup>63,64</sup>

### Examining Changes in Tau Aggregate Structure Profiles in the Context of Cryo-EM Tau Fibril Structures.

Current Cryo-EM tau fibril structures contain WT tau isoforms. Thus, we hypothesized that disease-associated mutations identified as forming alternate aggregate structures in our digestion assays may also be more likely to be incompatible with packing in the ordered fibril core. Mutagenesis analysis for disease-associated mutations was carried out in PyMOL on individual solved tau fibril structures for recombinant fibrils and patient-derived fibrils from Alzheimer and CBD samples.<sup>10,13,15,65,66</sup> For each structure, predicted steric clashes induced by mutation are reported in Table 2. Figure 4A maps the location of individual tau mutations and their predicted clashes in the context of the sequences solved in the Cryo-EM structures. We first focused on a fibril structure obtained by aggregation of recombinant tau termed the “snake” filament. All mutations predicted to cause a steric clash in our mutational analysis (N279K, deltaK280, L284R, deltaN296, S305I) also produced aggregate structure distinct from WT tau, supporting that these mutations are incompatible with the observed packing in the fibril structure. This was expected given these residues face toward the interface of  $\beta$ -strand packing interactions (Figure S6). However, we also found that the majority of mutations in the known ordered core region (with the exception of P301S and G303V) generated alternate structures to WT tau in our digest assay, despite inducing no detectable steric clash in our computational mutagenesis analysis. Most of the mutated residue sites face outward from the resolved packed core structure, and it is not readily clear how mutation at these sites would induce fibril structure changes (Figure S6). Our results could indicate that (1) our WT tau fibril structures are distinct from previously solved structures or (2) disease-associated mutations may act on the misfolding pathway upstream of fibril formation to alter the resulting aggregate structures produced (see discussion). Another key observation is that our mutant panel coverage extends beyond the solved regions for all current tau fibril structures. For example, the recombinant tau fibril structure termed the “snake filament” covers only 44% (16/36) of our examined mutations. Out of the mutations that lie outside the solved structure region, our digest fragment results suggest that 12/20 mutations induce the formation of structures distinct from WT tau. This raises the possibility that even though a mutation is not directly within the solved packed core structure, it may still influence core packing through distal interactions or induce local reproducible folding alterations in the more flexible regions of the aggregate core.

We also carried out an analysis of the compatibility of disease-associated mutations on structures determined for patient-derived fibrils (AD and CBD). In the AD paired helical filament (PHF) structure, G335S/V, Q336R, V337M, S352L, and G366R were predicted to cause clashes (Figure 4B).

Optimized structures of mutants templated onto AD PHF revealed additional potential incompatibilities. S305I, D348G, V363I, and E372G in addition to all of the previously noted mutants were predicted to have structural perturbations (Table S1). Similar to the recombinant tau fibril analysis, we observed all mutations (except G335V, D348G, and V363I) which were predicted to cause clashes formed alternate aggregate structures in our digest assays. As an example, for the V337M mutation linked to FTLD-tau in separate 3 families,<sup>67,68</sup> we predicted it caused potential steric clashes with all patient fibril structures examined: AD, CBD, and PSP<sup>67,68</sup> (steric clash shown for AD PHF in Figure 4C). Our digest assays indicate that V337M has the propensity to form non-WT aggregate structures. The finding that V337M and other mutations are not compatible with structures linked to WT tau tauopathies raises the possibility that their pathogenic properties may be due to their inherent propensity to form alternate aggregate structures that promote FTLD-tau specifically.

To gain more insight into the sequences present in the packed core region of our recombinant tau aggregates, we performed epitope mapping of trypsin-resistant fragments by capillary gel electrophoresis. We probed WT ON4R digest fragments with individual tau antibodies (Figure 4D). Differential positive or negative tau antibody reactivity and apparent MW of individual fragments were used to narrow the identity of the 10 kDa fragment to five potential sequence regions (Figure 4E). The five predicted sequences largely overlap with the most N-terminal sequence fragment covering residues 267–369 and the most C-terminal fragment covering residues 274–375. The finding that this 10 kDa fragment is consistent in our trypsin digest profile as one of the 3 major trypsin-resistant bands produced suggests that it is a main component of the protected core region of our aggregates. The predicted sequence coverage indicates that it is larger than the region solved by Cryo-EM for recombinant tau aggregates (272–330). The 10 kDa fragment more closely aligns with trypsin-resistant core sequences identified for patient-derived fibrils in CBD (268–369/387/395), PSP (260/268–395), or genetic FTLD-tau (268–369/387/395).<sup>7</sup> It also overlaps with highly GluC-resistant sequence regions (223–380) reported for 1N4R recombinant tau fibrils.<sup>6</sup>

There remains much to be learned about how tau is able to misfold and aggregate into the multiple amyloid core conformations observed in tauopathies and how tau's primary sequence contributes to specific misfolding events. Our current study takes advantage of missense mutations in tau linked to tauopathies to shed insight into the formation of specific tau aggregate structures. We reveal that single missense mutations introduced into human full-length ON4R tau are sufficient to modulate its misfolding pathway *in vitro*, leading to the production of alternate aggregate structures. The high-throughput tau purification platform we developed allowed us to perform direct comparisons of 36 tau mutants and WT tau with respect to their aggregate properties: structure and kinetics. We demonstrate the ability of a subset of tau mutations to inherently modulate tau aggregate structure formation, defining 13 distinct tau aggregate structure profiles within our panel. Our results offer a view into the complexity of the relationship between tau primary sequence and aggregation and provide a roadmap with which to systematically begin to dissect the fundamental principles underlying tau misfolding and aggregation.

Several atomic resolution structures have been determined for tau fibrils derived from tauopathies. However, the ability to perform similar studies in the case of familial tau mutations linked to tauopathies are limited by the extremely rare incidence of these mutations in general, with some mutations being reported in as few as 2 cases<sup>69,70</sup> (e.g., deltaK280). Our *in vitro* methods with recombinant tau protein provide an opportunity to directly test how tau mutations modulate aggregate structure formation under controlled and consistent conditions. The current study specifically examined the effects of tau mutations in the context of the 0N4R tau isoform. The results form a foundation in which to test other variables that may influence tau aggregate structure formation. For example, six tau isoforms are normally expressed in the neurons of the adult CNS<sup>71</sup> and it will be interesting to test if tau mutation effects on aggregate structure are applicable across all isoforms or behave similarly in aggregation reactions where multiple tau isoforms are present. Individual disease-associated tau mutations have been shown to cause tau aggregate pathology that consists primarily of 3R, 4R, or a mixture of tau isoforms.<sup>29,41</sup> In some cases, the inclusion of some tau isoforms but not others in aggregates may be caused by preferential expression of isoforms via mechanisms such as differential splicing.<sup>30–32</sup> However, another possibility is that some tau mutations drive isoform-specific promotion of pathogenic tau aggregate structures or ineffectively template some tau isoforms. This is plausible given that another group has already found differences in the packed core conformations between 1N3R and 1N4R heparin-induced aggregates including an additional protease protected C-terminal sequence region for 1N3R.<sup>6</sup> Tau aggregate structures can also be modulated by the accelerants<sup>72</sup> or buffer conditions<sup>73</sup> of the aggregation reaction. The packed fibril core of tau fibrils shows distinct conformations when aggregation is initiated by heparin,<sup>65</sup> RNA,<sup>73,74</sup> or phosphoserine.<sup>73</sup> Using our assays, we can begin to tease out the relative contributions of tau primary sequence and other additional cofactors, which may offer additional insight into how tau aggregation can be triggered in living cells.

In this study, we do not address the potential interplay between tau disease-associated mutations and post-translational modifications (PTMs) on modulating the formation of alternate aggregate structures. Tau has over 100 identified PTMs grouped in multiple categories such as phosphorylation, acetylation, methylation, glycosylation, proteolysis, and ubiquitination (for recent reviews, see refs 76,77). Hyperphosphorylation and individual phosphorylated sites are examples of PTM changes that have been linked to tau aggregate pathology in tauopathies. *In vitro* studies have demonstrated that the introduction of PTMs to tau can modulate its aggregation propensity.<sup>78–81</sup> However, there is evidence that the tau PTM landscape in tauopathies is complex. For example, heterogeneous mixtures of multiple PTMs are detected within cellular tau populations isolated from Alzheimer's Disease patients and the associated PTM patterns vary according to disease stage.<sup>75</sup> Moreover, it is currently difficult to discriminate which tau PTMs directly promote aggregation versus PTMs occurring on aggregated structures. Thus, future efforts should explore the degree to which our observed disease-associated mutation-induced effects on aggregate structure can be reinforced or neutralized in the context of the presence of individual PTMs (or PTM combinations).

We chose trypsin to identify changes in the protease resistance of tau aggregates because the high incidence of regularly spaced lysine and arginine residues throughout the tau sequence (Figure S3A) made it a sensitive indicator of structure changes that could be easily mapped. A potential caveat of our trypsin digest experiments is that multiple disease-associated mutations involve changes to or from lysine(K) and arginine(R) residues. Thus, it is possible that new aggregate structure profiles could be the result of gain or loss of a trypsin cleavage site. However, our data does not support this as being a general effect of K/R mutations. First, multiple mutations spread across different locations in tau (e.g., K298E, K317M, G366R, K369I) can produce the same trypsin-resistant profile binned as structure group 4 (SG4). Second, mutations such as L315R and Q336R introduce a new tryptic site located in the middle of the sequence of all available Cryo-EM structures as well as the 10 kDa fragment (residues within 267–375) identified in our WT tau digestion profile. Yet, a banding pattern reflective of trypsin digestion at this newly introduced site, which would essentially cleave the 10 kDa band into two smaller fragments, is not observed (Figure S7). Thus, we contend that tau mutants in our study involving K or R mutations can modulate tau aggregate core packing leading to the observed changes in protease-resistant profiles.

An unexpected finding from our study is that the effects of mutations on aggregate structures are not readily reconciled with current atomic resolution structure data on recombinant tau fibrils.<sup>65</sup> Several tau mutations that were predicted to be compatible with the fibril core solved by Cryo-EM generated aggregate structures distinguishable from those of WT. Moreover, tau mutations outside the region of the solved core structure were also found to alter aggregate structure formation. There could be several reasons to explain these discrepancies. Cryo-EM structures of recombinant tau induced in the presence of heparin use the 2N4R tau isoform.<sup>65</sup> It is possible that the specific tau isoform or other reaction conditions used in the previous study lead to an aggregate structure distinct from those generated by our conditions. Another possibility is that tau mutations alter upstream misfolding events that shuttle the misfolding pathway toward the production of alternate aggregate structures. In the case of tau mutations located outside the solved packed core region, we also postulate that mutation effects could be due to changes in the packing in more open and flexible structured regions of fibrils. For WT 0N4R tau, we mapped our 10 kDa fragment to a region within residues 267–375. All but two of the tau mutations that altered the aggregate structure (I260V and R406W) in this study are contained within this region. Thus, our results offer new insights into how tau's primary sequence may contribute to shaping the tau aggregate structure in regions not yet resolvable by techniques such as Cryo-EM.

Using our new high-throughput methods for tau purification and our trypsin digest assay for comparing aggregate structures, we hope to assist in defining the complex relationships between tau sequence, aggregate properties, and the biological effects of aggregates at the cellular and *in vivo* levels. Multiple factors can contribute to the pathogenicity of a disease-associated tau mutation. Tau mutations such as P301L enhance the propensity of tau to aggregate, however, this is not the case for other tau mutations linked to tauopathy. Our results open up the possibility that tau mutations with WT-like or slow aggregation kinetics may be pathogenic, in part, via their ability to assemble into alternate tau aggregate structures.

Disease-associated tau mutations are a common element of current cell and animal model systems used to study tau misfolding. Our work reveals that the choice of mutation influences the overall misfolding process and may need to be considered when designing future studies. Future characterization comparing the ability of distinct tau aggregate structures to promote seeding, propagation, and evade protein quality control factors will dissect the fundamental features of tau aggregates responsible for their induced pathobiology.

## METHODS

**Cloning of Tau Constructs.** Mimics of disease-associated tau mutations were generated in the 0N4R isoform of human tau by site-directed mutagenesis. The parent vector is pET28 0N4R which encodes for expression of WT 0N4R tau that is N-terminally fused to a sequence containing a 6X-His-tag and a thrombin cleavage site. Q5 polymerase (NEB) was used to amplify the pET28 0N4R plasmid<sup>46</sup> with desired mutagenesis primer pairs. Amplified templates were treated with DpnI (Thermo Fisher) prior to transformation into DH5 $\alpha$  competent cells (Agilent). Successful mutation of isolated clones was verified by Sanger sequencing, and clones were retransformed into BL21-CodonPlus (DE3)-RP competent cells (Agilent) for protein expression.

**Tau Purification.** Large-scale protein purifications of tau were carried out as previously described in Mok et al.<sup>46</sup> The large-scale purification protocol was modified as followed for small-scale protein expression and purification. Cells transformed with individual tau variants were grown to an O.D. 600 of 0.7 and then induced with IPTG (500  $\mu$ M) for 3 h at 30 °C to allow for protein expression. Pelleted cells arrayed in 96-well plates were resuspended in resuspension buffer (1.5 mM KH<sub>2</sub>PO<sub>4</sub>, 8 mM Na<sub>2</sub>HPO<sub>4</sub>, 2.7 mM KCl, 2 mM DTT, 2 mM PMSF, pH 7.2) then lysed with lysozyme (0.3 mg/mL final) in 3 successive freeze–thaw cycles. Lysates were treated with 12 U/mL of Benzonase for 30 min at 4 °C, boiled for 20 min, and cleared by 2 rounds of centrifugation at 3214g for 15 min in 96-deep-well plates. Tau was purified from the supernatant fraction by in-well chromatography using SP ImpRes/SP sepharose FF resin (Cytiva) incubated in 96-well filter plates (Supor PES membrane 1.2  $\mu$ M, Pall). Following 4 rounds of buffer exchange in wash buffer (1.5 mM KH<sub>2</sub>PO<sub>4</sub>, 8 mM Na<sub>2</sub>HPO<sub>4</sub>, 2.7 mM KCl, 2 mM DTT, 50–150 mM NaCl, pH 7.2), tau was eluted in elution buffer (1.5 mM KH<sub>2</sub>PO<sub>4</sub>, 8 mM Na<sub>2</sub>HPO<sub>4</sub>, 2.7 mM KCl, 2 mM DTT, 350 mM NaCl, pH 7.2). Eluted tau protein was subject to buffer exchange in low-salt buffer (1.5 mM KH<sub>2</sub>PO<sub>4</sub>, 8 mM Na<sub>2</sub>HPO<sub>4</sub>, 2.7 mM KCl, 2 mM DTT, pH 7.2) and then aggregation assay buffer (Dulbecco's PBS, pH 7.4, 2 mM DTT) using 3K MWCO filter plates (Pall). Buffer exchange was monitored by measuring the conductivity of the protein sample with a conductivity probe calibrated to standard solutions (INLAB 751–4MM, Mettler Toledo). Concentrations of purified tau protein were determined using a reducing agent compatible bicinchoninic acid (BCA) assay (Thermo Fisher). Protein purity of final preparations was assessed by coomassie-stained SDS-PAGE or MALDI-TOF Mass spectrometry (Bruker Autoflex Speed MALDI-ToF, Bruker Daltonic).

**Tau Kinetic Aggregation Assays.** Aggregation kinetic assays were performed and analyzed as previously described.<sup>46</sup> Briefly, reactions consisted of 10  $\mu$ M tau, 10  $\mu$ M thioflavin T (Sigma), and 44  $\mu$ g/mL heparin sodium salt (Santa Cruz) in assay buffer. Aggregation reactions were carried out at 37 °C with continuous shaking and monitored via ThT fluorescence (excitation, 444 nm; emission, 485 nm; cutoff, 480 nm) in a Spectramax M5 microplate reader (Molecular Devices). Readings were taken every 5 min for a minimum of 24 h. For analysis of kinetic aggregation curves, individual baseline subtracted curves were fitted to the Gompertz function<sup>82,83</sup> to extract kinetic parameters (lag time, amyloid formation rate constant, amplitude). A weighting of 1/Y was applied during the fitting to accurately capture the lag time values.

**Trypsin Digestion of Tau Aggregates.** Tau aggregates directly sampled from *in vitro* aggregation assays (15  $\mu$ L) were treated with a

final concentration of 0.03 mg/mL mass-spectrometry-grade trypsin (Thermo Fisher) in D-PBS. A time course digestion using WT 0N4R tau as the substrate was performed for each trypsin lot to calibrate assay conditions (total digestion time) across experiments. Trypsin digest assays were incubated at 37 °C with shaking at 800 rpm for the indicated times. Digestion reactions were stopped by the addition of sample buffer (Fluorescent Master Mix, ProteinSimple) and heating to 95 °C for 5 min. Tau fragments were resolved using the Jess capillary gel electrophoresis system (ProteinSimple) with the 2–40 kDa separation module. Reagents and equipment were purchased from ProteinSimple unless stated otherwise. Four microliters of each sample were loaded into the top-row wells of plates preloaded with proprietary electrophoresis buffers designed to separate proteins of 2–40 kDa. Subsequent rows of the plate were filled with blocking buffer, primary and secondary antibody solutions, and chemiluminescence reagents, according to the manufacturer's instructions. Detection of protein fragments was performed with the total protein detection module or capillary Western blots using tau antibodies.<sup>84</sup> Primary antibodies were tau monoclonal antibodies including DA9 (aa 102–140, 1:10 dilution), ET3 (aa 273–288, 1:10 dilution),<sup>85</sup> and 77G7 (BioLegend, aa 316–355, 1:100 dilution). DA9 and ET3 antibodies were generously provided by Peter Davies. Secondary antibodies were anti-mouse secondary HRP used according to manufacturer's directions (ProteinSimple). CompassSW software (ProteinSimple) was used to generate chromatograms representing the lane profiles of separated protease-resistant tau fragments detected by using the total protein module (ProteinSimple) or tau antibodies. Chromatograms plot signal intensity versus apparent MW, calibrated using protein standards included in each capillary run.

**Comparative Analysis of Trypsin-Resistant Tau Fragment Profiles.** To perform a cross-comparison of chromatograms (fragment banding patterns), a normalization step was first conducted to generate standardized increment values with respect to kDa across all chromatograms. Namely, from each profile, a 1-D function is interpolated, and values in the range from 6 to 24 with a step of 0.1 are obtained, see Figure S8.

Subsequently, the distance among the interpolated profiles is obtained by computing the correlation distance. Given two 1-D arrays,  $u$  and  $v$ , the correlation distance between  $u$  and  $v$  is defined as

$$d(u, v) = 1 - \frac{(u - \bar{u}) \cdot (v - \bar{v})}{\| (u - \bar{u}) \|_2 \| (v - \bar{v}) \|_2}$$

where  $\bar{u}$  is the mean value of the elements of  $u$  and  $x \cdot y$  is the dot product of  $x$  and  $y$ . Once the distance among the profiles is computed, they are grouped by hierarchical clustering using average linkage (this is represented by means of a dendrogram)<sup>86</sup> and the distance among the samples is graphically shown by using a heatmap. This process has been implemented in the Python programming language and using the scikit-learn<sup>87</sup> and scipy<sup>88</sup> libraries.

**Epitope Mapping of Trypsin-Resistant Tau Fragments.** A script was generated in the Python programming language to identify potential tau sequences corresponding to individual trypsin-resistant tau fragments based on their reactivity to assayed tau antibodies and their apparent MW via capillary gel electrophoresis. The script identifies potential tau fragment sequences generated by trypsin digestion for a given MW. It then includes or excludes potential sequences based on their reactivity with assayed tau antibodies. The program also searches for potential tau dimer sequences if no matching sequence is predicted from the initial analysis.

**Dot Blots.** 0N4R and 0N3R WT tau were expressed and purified in alternating wells of a 96-well plate by small-scale tau expression and purification. 100 pmol of purified tau sample from each well was applied directly to a 0.1  $\mu$ m nitrocellulose blotting membrane. The membrane was probed with primary antibodies including tau mouse ET3 (1:1000 dilution) and 6X-His Tag rabbit monoclonal antibody (Invitrogen, 1:3500 dilution). The secondary antibodies used were Cytiva CyDye 700 goat-anti-mouse and Cytiva CyDye 800 goat-anti-mouse (diluted 1:10 000). Following secondary antibody incubation,

the blot was visualized with a LICOR imager using the 700 and 800 nm channels.

**MALDI-TOF.** For MALDI analysis, 1  $\mu\text{L}$  of each sample was mixed with 1  $\mu\text{L}$  of sinapinic acid (10 mg/mL in 50% acetonitrile/water + 0.1% trifluoroacetic acid). 1  $\mu\text{L}$  portion of the sample/matrix solution was then spotted onto a stainless steel target plate and allowed to air-dry. Mass spectra were obtained using a Bruker Autoflex Speed MALDI-TOF instrument (Bruker Daltonic GmbH). All MS spectra were recorded in positive linear mode, and external calibration was performed by use of a standard protein mixture. Predicted  $m/z$  for full-length protein: 43801.1696 (with met oxidation = 43961.1188).

**Modeling Tau Mutations into Existing Cryo-EM Tau Fibril Structures.** PDB structures and their associated 2FoFc maps were modeled in PyMOL (AD SF: 5O3T, AD PHF: 6HRE, CBD: 6TJO, PSP: 7U0Z, snake: 6QJH, twister: 6QJM, jagged: 6QJP). Mutations were modeled onto structures using the mutagenesis function, and all backbone-dependent rotamers were analyzed. Amino acid mutations where all allowed side chain rotamers clash with the existing structure were deemed as incompatible. Optimized mutant structures for 6HRE were generated by substituting amino acid mutations into the primary sequence. Five cycles of PDB structures were generated using MODELLER with 6HRE as a template. RMSD was calculated with PyMOL's alignment function in comparison to 6HRE. The model with the lowest RMSD was selected for analysis.

## ■ ASSOCIATED CONTENT

### Data Availability Statement

All code described in the Methods section for processing data from aggregation kinetics, digest profile comparisons, and epitope mapping are available at the following GitHub repository: [https://github.com/sueannmok/tau\\_digest\\_and\\_kinetics\\_tools.git](https://github.com/sueannmok/tau_digest_and_kinetics_tools.git)

### SI Supporting Information

The Supporting Information is available free of charge at <https://pubs.acs.org/doi/10.1021/acschemneuro.3c00422>.

Example result for interpolation of capillary gel electrophoresis chromatogram; small-scale purification yields, purity, and aggregation kinetics; location of trypsin cut sites in tau construct; comparison of structure groups and changes in pI or hydrophobicity; correlation matrix heatmap and dendrogram used to define structure groups; kinetic aggregation parameters and relationship to structure group identification; location of tau mutations on Cryo-EM structure (PDB: 6QJH); representative capillary gel electrophoresis chromatograms (PDF)

## ■ AUTHOR INFORMATION

### Corresponding Author

Sue-Ann Mok – Department of Biochemistry, University of Alberta, Edmonton, Alberta, Canada T6G 2H7;

orcid.org/0000-0003-4593-3368; Email: [sueann@ualberta.ca](mailto:sueann@ualberta.ca)

### Authors

Kerry T. Sun – Department of Biochemistry, University of Alberta, Edmonton, Alberta, Canada T6G 2H7

Tark Patel – Department of Biochemistry, University of Alberta, Edmonton, Alberta, Canada T6G 2H7

Sang-Gyun Kang – Department of Biochemistry, University of Alberta, Edmonton, Alberta, Canada T6G 2H7;

orcid.org/0000-0002-6875-113X

Allan Yarahmady – Department of Biochemistry, University of Alberta, Edmonton, Alberta, Canada T6G 2H7;

orcid.org/0009-0008-0397-7294

Mahalashmi Srinivasan – Department of Biochemistry, University of Alberta, Edmonton, Alberta, Canada T6G 2H7

Olivier Julien – Department of Biochemistry, University of Alberta, Edmonton, Alberta, Canada T6G 2H7;

orcid.org/0000-0001-7068-7299

Jónathan Heras – Department of Mathematics and Computer Sciences, University of La Rioja, Logroño, Spain 26004;

orcid.org/0000-0003-4775-1306

Complete contact information is available at:

<https://pubs.acs.org/10.1021/acschemneuro.3c00422>

### Author Contributions

K.T.S., T.P., J.H., A.Y., and S.-A.M. conceived and designed the study. K.T.S., T.P., S.-G.K., J.H., O.J., M.S., and A.Y. acquired, analyzed, or interpreted data. K.T.S., T.P., S.-G.K., M.S., O.J., J.H., and S.-A.M. drafted and revised the manuscript.

### Notes

The authors declare no competing financial interest.

## ■ ACKNOWLEDGMENTS

The authors thank Ghazaleh Eskandari-Sedighi and Andrew Castle for advice regarding capillary gel electrophoresis, and Jack Moore of the Alberta Proteomics and Mass Spectrometry Facility (University of Alberta) for assistance with mass spectrometry sample preparation and data analysis. They also thank Peter Davies for generously providing tau antibodies used in this study. They thank Richard Fahlman and Valerie Sim for critical discussions of the project during its development. This work was funded by the following grants to S.-A.M. from Alberta Innovates, the Alzheimer's Society of Alberta and Northwest Territories, and donors of the ADR; a program of the BrightFocus Foundation (A2022044S), to S.-A.M. (RGPIN-2019-06230) and O.J. (RGPIN-2018-05881) from NSERC, and to J.H. (PID2020-115225RB-I00 funded by MCIN/AEI/10.13039/501100011033). K.T.S. was supported by a Canada Graduate Scholarship-Master's (CIHR).

## ■ REFERENCES

- (1) Kovacs, G. G. Tauopathies. In *Handbook of Clinical Neurology*; Elsevier, 2018; Vol. 145, pp 355–368 DOI: 10.1016/B978-0-12-802395-2.00025-0.
- (2) Lee, V. M.-Y.; Goedert, M.; Trojanowski, J. Q. Neurodegenerative Tauopathies. *Annu. Rev. Neurosci.* **2001**, *24* (1), 1121–1159.
- (3) Wegmann, S.; Medalsy, I. D.; Mandelkow, E.; Müller, D. J. The Fuzzy Coat of Pathological Human Tau Fibrils Is a Two-Layered Polyelectrolyte Brush. *Proc. Natl. Acad. Sci. U.S.A.* **2013**, *110* (4), E313–E321.
- (4) Barghorn, S.; Davies, P.; Mandelkow, E. Tau Paired Helical Filaments from Alzheimer's Disease Brain and Assembled in Vitro Are Based on  $\beta$ -Structure in the Core Domain. *Biochemistry* **2004**, *43* (6), 1694–1703.
- (5) Wischik, C. M.; Novak, M.; Edwards, P. C.; Klug, A.; Tichelaar, W.; Crowther, R. A. Structural Characterization of the Core of the Paired Helical Filament of Alzheimer Disease. *Proc. Natl. Acad. Sci. U.S.A.* **1988**, *85* (13), 4884–4888.
- (6) Caroux, E.; Redeker, V.; Madiona, K.; Melki, R. Structural Mapping Techniques Distinguish the Surfaces of Fibrillar 1N3R and 1N4R Human Tau. *J. Biol. Chem.* **2021**, *297* (5), No. 101252.
- (7) Taniguchi-Watanabe, S.; Arai, T.; Kametani, F.; Nonaka, T.; Masuda-Suzukake, M.; Tarutani, A.; Murayama, S.; Saito, Y.; Arima, K.; Yoshida, M.; Akiyama, H.; Robinson, A.; Mann, D. M. A.; Iwatsubo, T.; Hasegawa, M. Biochemical Classification of Tauopathies by Immunoblot, Protein Sequence and Mass Spectrometry

Analyses of Sarkosyl-Insoluble and Trypsin-Resistant Tau. *Acta Neuropathol.* **2016**, *131* (2), 267–280.

(8) Hasegawa, M.; Watanabe, S.; Kondo, H.; Akiyama, H.; Mann, D. M. A.; Saito, Y.; Murayama, S. 3R and 4R Tau Isoforms in Paired Helical Filaments in Alzheimer's Disease. *Acta Neuropathol.* **2014**, *127* (2), 303–305.

(9) Jakes, R.; Novak, M.; Davison, M.; Wischik, C. M. Identification of 3- and 4-Repeat Tau Isoforms within the PHF in Alzheimer's Disease. *EMBO J.* **1991**, *10* (10), 2725–2729.

(10) Falcon, B.; Zhang, W.; Schweighauser, M.; Murzin, A. G.; Vidal, R.; Garringer, H. J.; Ghetti, B.; Scheres, S. H. W.; Goedert, M. Tau Filaments from Multiple Cases of Sporadic and Inherited Alzheimer's Disease Adopt a Common Fold. *Acta Neuropathol.* **2018**, *136* (5), 699–708.

(11) Falcon, B.; Zhang, W.; Murzin, A. G.; Murshudov, G.; Garringer, H. J.; Vidal, R.; Crowther, R. A.; Ghetti, B.; Scheres, S. H. W.; Goedert, M. Structures of Filaments from Pick's Disease Reveal a Novel Tau Protein Fold. *Nature* **2018**, *561* (7721), 137–140.

(12) Falcon, B.; Zivanov, J.; Zhang, W.; Murzin, A. G.; Garringer, H. J.; Vidal, R.; Crowther, R. A.; Newell, K. L.; Ghetti, B.; Goedert, M.; Scheres, S. H. W. Novel Tau Filament Fold in Chronic Traumatic Encephalopathy Encloses Hydrophobic Molecules. *Nature* **2019**, *568* (7752), 420–423.

(13) Zhang, W.; Tarutani, A.; Newell, K. L.; Murzin, A. G.; Matsubara, T.; Falcon, B.; Vidal, R.; Garringer, H. J.; Shi, Y.; Ikeuchi, T.; Murayama, S.; Ghetti, B.; Hasegawa, M.; Goedert, M.; Scheres, S. H. W. Novel Tau Filament Fold in Corticobasal Degeneration. *Nature* **2020**, *580* (7802), 283–287.

(14) Shi, Y.; Zhang, W.; Yang, Y.; Murzin, A. G.; Falcon, B.; Kotecha, A.; van Beers, M.; Tarutani, A.; Kametani, F.; Garringer, H. J.; Vidal, R.; Hallinan, G. I.; Lashley, T.; Saito, Y.; Murayama, S.; Yoshida, M.; Tanaka, H.; Kakita, A.; Ikeuchi, T.; Robinson, A. C.; Mann, D. M. A.; Kovacs, G. G.; Revesz, T.; Ghetti, B.; Hasegawa, M.; Goedert, M.; Scheres, S. H. W. Structure-Based Classification of Tauopathies. *Nature* **2021**, *598* (7880), 359–363.

(15) Fitzpatrick, A. W. P.; Falcon, B.; He, S.; Murzin, A. G.; Murshudov, G.; Garringer, H. J.; Crowther, R. A.; Ghetti, B.; Goedert, M.; Scheres, S. H. W. Cryo-EM Structures of Tau Filaments from Alzheimer's Disease. *Nature* **2017**, *547* (7662), 185–190.

(16) Frost, B.; Diamond, M. I. Prion-like Mechanisms in Neurodegenerative Diseases. *Nat. Rev. Neurosci.* **2010**, *11* (3), 155–159.

(17) Dujardin, S.; Hyman, B. T. Tau Prion-Like Propagation: State of the Art and Current Challenges. In *Tau Biology*; Takashima, A.; Wolozin, B.; Buee, L., Eds.; Advances in Experimental Medicine and Biology; Springer Singapore: Singapore, 2019; Vol. 1184, pp 305–325.

(18) Clavaguera, F.; Bolmont, T.; Crowther, R. A.; Abramowski, D.; Frank, S.; Probst, A.; Fraser, G.; Stalder, A. K.; Beibel, M.; Staufenbiel, M.; Jucker, M.; Goedert, M.; Tolnay, M. Transmission and Spreading of Tauopathy in Transgenic Mouse Brain. *Nat. Cell Biol.* **2009**, *11* (7), 909–913.

(19) Sanders, D. W.; Kaufman, S. K.; DeVos, S. L.; Sharma, A. M.; Mirbaha, H.; Li, A.; Barker, S. J.; Foley, A. C.; Thorpe, J. R.; Serpell, L. C.; Miller, T. M.; Grinberg, L. T.; Seeley, W. W.; Diamond, M. I. Distinct Tau Prion Strains Propagate in Cells and Mice and Define Different Tauopathies. *Neuron* **2014**, *82* (6), 1271–1288.

(20) Kaufman, S. K.; Sanders, D. W.; Thomas, T. L.; Ruchinskas, A. J.; Vaquer-Alicea, J.; Sharma, A. M.; Miller, T. M.; Diamond, M. I. Tau Prion Strains Dictate Patterns of Cell Pathology, Progression Rate, and Regional Vulnerability In Vivo. *Neuron* **2016**, *92* (4), 796–812.

(21) Guo, J. L.; Narasimhan, S.; Changolkar, L.; He, Z.; Stieber, A.; Zhang, B.; Gathagan, R. J.; Iba, M.; McBride, J. D.; Trojanowski, J. Q.; Lee, V. M. Y. Unique Pathological Tau Conformers from Alzheimer's Brains Transmit Tau Pathology in Nontransgenic Mice. *J. Exp. Med.* **2016**, *213* (12), 2635–2654.

(22) Woerman, A. L.; Aoyagi, A.; Patel, S.; Kazmi, S. A.; Lobach, I.; Grinberg, L. T.; McKee, A. C.; Seeley, W. W.; Olson, S. H.; Prusiner,

S. B. Tau Prions from Alzheimer's Disease and Chronic Traumatic Encephalopathy Patients Propagate in Cultured Cells. *Proc. Natl. Acad. Sci. U.S.A.* **2016**, *113* (50), E8187–E8196.

(23) Narasimhan, S.; Guo, J. L.; Changolkar, L.; Stieber, A.; McBride, J. D.; Silva, L. V.; He, Z.; Zhang, B.; Gathagan, R. J.; Trojanowski, J. Q.; Lee, V. M. Y. Pathological Tau Strains from Human Brains Recapitulate the Diversity of Tauopathies in Nontransgenic Mouse Brain. *J. Neurosci. Off. J. Soc. Neurosci.* **2017**, *37* (47), 11406–11423.

(24) Ghetti, B.; Oblak, A. L.; Boeve, B. F.; Johnson, K. A.; Dickerson, B. C.; Goedert, M. Invited Review: Frontotemporal Dementia Caused by Microtubule-Associated Protein Tau Gene (MAPT) Mutations: A Chameleon for Neuropathology and Neuroimaging. *Neuropathol. Appl. Neurobiol.* **2015**, *41* (1), 24–46.

(25) Pottier, C.; Ravenscroft, T. A.; Sanchez-Contreras, M.; Rademakers, R. Genetics of FTL: Overview and What Else We Can Expect from Genetic Studies. *J. Neurochem.* **2016**, *138* (Suppl 1), 32–53.

(26) Forrest, S. L.; Halliday, G. M.; McCann, H.; McGeachie, A. B.; McGinley, C. V.; Hodges, J. R.; Piguat, O.; Kwok, J. B.; Spillantini, M. G.; Kril, J. J. Heritability in Frontotemporal Tauopathies. *Alzheimer's Dement.* **2019**, *11*, 115–124.

(27) Moore, K. M.; Nicholas, J.; Grossman, M.; McMillan, C. T.; Irwin, D. J.; Massimo, L.; Van Deerlin, V. M.; Warren, J. D.; Fox, N. C.; Rossor, M. N.; Mead, S.; Bocchetta, M.; Boeve, B. F.; Knopman, D. S.; Graff-Radford, N. R.; Forsberg, L. K.; Rademakers, R.; Wszolek, Z. K.; van Swieten, J. C.; Jiskoot, L. C.; Meeter, L. H.; Dopfer, E. G.; Papma, J. M.; Snowden, J. S.; Saxon, J.; Jones, M.; Pickering-Brown, S.; Le Ber, I.; Camuzat, A.; Brice, A.; Caroppo, P.; Ghidoni, R.; Pievani, M.; Benussi, L.; Binetti, G.; Dickerson, B. C.; Lucente, D.; Krivensky, S.; Graff, C.; Öijerstedt, L.; Fallström, M.; Thonberg, H.; Ghoshal, N.; Morris, J. C.; Borroni, B.; Benussi, A.; Padovani, A.; Galimberti, D.; Scarpini, E.; Fumagalli, G. G.; Mackenzie, I. R.; Hsiung, G.-Y. R.; Sengdy, P.; Boxer, A. L.; Rosen, H.; Taylor, J. B.; Synofzik, M.; Wilke, C.; Sulzer, P.; Hodges, J. R.; Halliday, G.; Kwok, J.; Sanchez-Valle, R.; Lladó, A.; Borrego-Ecija, S.; Santana, I.; Almeida, M. R.; Tábuas-Pereira, M.; Moreno, F.; Barandiaran, M.; Indakoetxea, B.; Levin, J.; Danek, A.; Rowe, J. B.; Cope, T. E.; Otto, M.; Anderl-Straub, S.; de Mendonça, A.; Maruta, C.; Masellis, M.; Black, S. E.; Couratier, P.; Lautrette, G.; Huey, E. D.; Sorbi, S.; Nacmias, B.; Laforce, R.; Tremblay, M.-P. L.; Vandenberghe, R.; Damme, P. V.; Rogalski, E. J.; Weintraub, S.; Gerhard, A.; Onyike, C. U.; Ducharme, S.; Papageorgiou, S. G.; Ng, A. S. L.; Brodtmann, A.; Finger, E.; Guerreiro, R.; Bras, J.; Rohrer, J. D.; Prevention Initiative, F. T. D.; et al. Age at Symptom Onset and Death and Disease Duration in Genetic Frontotemporal Dementia: An International Retrospective Cohort Study. *Lancet Neurol.* **2020**, *19* (2), 145–156.

(28) Young, A. L.; Bocchetta, M.; Russell, L. L.; Convery, R. S.; Peakman, G.; Todd, E.; Cash, D. M.; Greaves, C. V.; van Swieten, J.; Jiskoot, L.; Seelaar, H.; Moreno, F.; Sanchez-Valle, R.; Borroni, B.; Laforce, R.; Masellis, M.; Tartaglia, M. C.; Graff, C.; Galimberti, D.; Rowe, J. B.; Finger, E.; Synofzik, M.; Vandenberghe, R.; de Mendonça, A.; Tagliavini, F.; Santana, I.; Ducharme, S.; Butler, C.; Gerhard, A.; Levin, J.; Danek, A.; Otto, M.; Sorbi, S.; Williams, S. C. R.; Alexander, D. C.; Rohrer, J. D.; on behalf of the Genetic FTDP Initiative (GENFI). Characterizing the Clinical Features and Atrophy Patterns of MAPT-Related Frontotemporal Dementia With Disease Progression Modeling. *Neurology* **2021**, *97* (9), e941–e952.

(29) Forrest, S. L.; Kril, J. J.; Stevens, C. H.; Kwok, J. B.; Hallupp, M.; Kim, W. S.; Huang, Y.; McGinley, C. V.; Werka, H.; Kiernan, M. C.; Götz, J.; Spillantini, M. G.; Hodges, J. R.; Ittner, L. M.; Halliday, G. M. Retiring the Term FTDP-17 as MAPT Mutations Are Genetic Forms of Sporadic Frontotemporal Tauopathies. *Brain* **2018**, *141* (2), 521–534.

(30) Varani, L.; Hasegawa, M.; Spillantini, M. G.; Smith, M. J.; Murrell, J. R.; Ghetti, B.; Klug, A.; Goedert, M.; Varani, G. Structure of Tau Exon 10 Splicing Regulatory Element RNA and Destabilization by Mutations of Frontotemporal Dementia and Parkinsonism

- Linked to Chromosome 17. *Proc. Natl. Acad. Sci. U.S.A.* **1999**, *96* (14), 8229–8234.
- (31) D'Souza, I.; Poorkaj, P.; Hong, M.; Nochlin, D.; Lee, V. M.; Bird, T. D.; Schellenberg, G. D. Missense and Silent Tau Gene Mutations Cause Frontotemporal Dementia with Parkinsonism-Chromosome 17 Type, by Affecting Multiple Alternative RNA Splicing Regulatory Elements. *Proc. Natl. Acad. Sci. U.S.A.* **1999**, *96* (10), 5598–5603.
- (32) Hasegawa, M.; Smith, M. J.; Iijima, M.; Tabira, T.; Goedert, M. FTDP-17 Mutations N279K and S305N in Tau Produce Increased Splicing of Exon 10. *FEBS Lett.* **1999**, *443* (2), 93–96.
- (33) Barghorn, S.; Zheng-Fischhöfer, Q.; Ackmann, M.; Biernat, J.; von Bergen, M.; Mandelkow, E. M.; Mandelkow, E. Structure, Microtubule Interactions, and Paired Helical Filament Aggregation by Tau Mutants of Frontotemporal Dementias. *Biochemistry* **2000**, *39* (38), 11714–11721.
- (34) Goedert, M.; Jakes, R.; Crowther, R. A. Effects of Frontotemporal Dementia FTDP-17 Mutations on Heparin-Induced Assembly of Tau Filaments. *FEBS Lett.* **1999**, *450* (3), 306–311.
- (35) Combs, B.; Gamblin, T. C. FTDP-17 Tau Mutations Induce Distinct Effects on Aggregation and Microtubule Interactions. *Biochemistry* **2012**, *51* (43), 8597–8607.
- (36) Kfoury, N.; Holmes, B. B.; Jiang, H.; Holtzman, D. M.; Diamond, M. I. Trans-Cellular Propagation of Tau Aggregation by Fibrillar Species. *J. Biol. Chem.* **2012**, *287* (23), 19440–19451.
- (37) Strang, K. H.; Croft, C. L.; Sorrentino, Z. A.; Chakrabarty, P.; Golde, T. E.; Giasson, B. I. Distinct Differences in Prion-like Seeding and Aggregation between Tau Protein Variants Provide Mechanistic Insights into Tauopathies. *J. Biol. Chem.* **2018**, *293* (7), 2408–2421.
- (38) Fischer, D.; Mukrasch, M. D.; von Bergen, M.; Klos-Witkowska, A.; Biernat, J.; Griesinger, C.; Mandelkow, E.; Zweckstetter, M. Structural and Microtubule Binding Properties of Tau Mutants of Frontotemporal Dementias. *Biochemistry* **2007**, *46* (10), 2574–2582.
- (39) LeBoeuf, A. C.; Levy, S. F.; Gaylord, M.; Bhattacharya, A.; Singh, A. K.; Jordan, M. A.; Wilson, L.; Feinstein, S. C. FTDP-17 Mutations in Tau Alter the Regulation of Microtubule Dynamics: An “Alternative Core” Model for Normal and Pathological Tau Action. *J. Biol. Chem.* **2008**, *283* (52), 36406–36415.
- (40) Xia, Y.; Sorrentino, Z. A.; Kim, J. D.; Strang, K. H.; Riffe, C. J.; Giasson, B. I. Impaired Tau-Microtubule Interactions Are Prevalent among Pathogenic Tau Variants Arising from Missense Mutations. *J. Biol. Chem.* **2019**, *294* (48), 18488–18503.
- (41) Hong, M.; Zhukareva, V.; Vogelsberg-Ragaglia, V.; Wszolek, Z.; Reed, L.; Miller, B. I.; Geschwind, D. H.; Bird, T. D.; McKeel, D.; Goate, A.; Morris, J. C.; Wilhelmsen, K. C.; Schellenberg, G. D.; Trojanowski, J. Q.; Lee, V. M. Mutation-Specific Functional Impairments in Distinct Tau Isoforms of Hereditary FTDP-17. *Science* **1998**, *282* (5395), 1914–1917.
- (42) Gunawardana, C. G.; Mehrabian, M.; Wang, X.; Mueller, I.; Lubambo, I. B.; Jonkman, J. E. N.; Wang, H.; Schmitt-Ulms, G. The Human Tau Interactome: Binding to the Ribonucleoproteome, and Impaired Binding of the Proline-to-Leucine Mutant at Position 301 (P301L) to Chaperones and the Proteasome. *Mol. Cell. Proteomics* **2015**, *14* (11), 3000–3014.
- (43) Tracy, T. E.; Madero-Pérez, J.; Swaney, D. L.; Chang, T. S.; Moritz, M.; Konrad, C.; Ward, M. E.; Stevenson, E.; Hüttenhain, R.; Kauwe, G.; Mercedes, M.; Sweetland-Martin, L.; Chen, X.; Mok, S.-A.; Wong, M. Y.; Telpoukhovskaia, M.; Min, S.-W.; Wang, C.; Sohn, P. D.; Martin, J.; Zhou, Y.; Luo, W.; Trojanowski, J. Q.; Lee, V. M. Y.; Gong, S.; Manfredi, G.; Coppola, G.; Krogan, N. J.; Geschwind, D. H.; Gan, L. Tau Interactome Maps Synaptic and Mitochondrial Processes Associated with Neurodegeneration. *Cell* **2022**, *185* (4), 712–728e14.
- (44) Dayanandan, R.; Van Slegtenhorst, M.; Mack, T. G.; Ko, L.; Yen, S. H.; Leroy, K.; Brion, J. P.; Anderton, B. H.; Hutton, M.; Lovestone, S. Mutations in Tau Reduce Its Microtubule Binding Properties in Intact Cells and Affect Its Phosphorylation. *FEBS Lett.* **1999**, *446* (2–3), 228–232.
- (45) Kimura, T.; Hosokawa, T.; Taoka, M.; Tsutsumi, K.; Ando, K.; Ishiguro, K.; Hosokawa, M.; Hasegawa, M.; Hisanaga, S.-I. Quantitative and Combinatory Determination of *In Situ* Phosphorylation of Tau and Its FTDP-17 Mutants. *Sci. Rep.* **2016**, *6*, No. 33479.
- (46) Mok, S.-A.; Condello, C.; Freilich, R.; Gillies, A.; Arhar, T.; Oroz, J.; Kadavath, H.; Julien, O.; Assimon, V. A.; Rauch, J. N.; Dunyak, B. M.; Lee, J.; Tsai, F. T. F.; Wilson, M. R.; Zweckstetter, M.; Dickey, C. A.; Gestwicki, J. E. Mapping Interactions with the Chaperone Network Reveals Factors That Protect against Tau Aggregation. *Nat. Struct. Mol. Biol.* **2018**, *25* (5), 384–393.
- (47) Caballero, B.; Wang, Y.; Diaz, A.; Tasset, I.; Juste, Y. R.; Stiller, B.; Mandelkow, E.-M.; Mandelkow, E.; Cuervo, A. M. Interplay of Pathogenic Forms of Human Tau with Different Autophagic Pathways. *Aging Cell* **2018**, *17* (1), No. e12692.
- (48) Mahali, S.; Martinez, R.; King, M.; Verbeck, A.; Harari, O.; Benitez, B. A.; Horie, K.; Sato, C.; Temple, S.; Karch, C. M. Defective Proteostasis in Induced Pluripotent Stem Cell Models of Frontotemporal Lobar Degeneration. *Transl. Psychiatry* **2022**, *12* (1), No. 508.
- (49) Sohn, P. D.; Huang, C. T.-L.; Yan, R.; Fan, L.; Tracy, T. E.; Camargo, C. M.; Montgomery, K. M.; Arhar, T.; Mok, S.-A.; Freilich, R.; Baik, J.; He, M.; Gong, S.; Roberson, E. D.; Karch, C. M.; Gestwicki, J. E.; Xu, K.; Kosik, K. S.; Gan, L. Pathogenic Tau Impairs Axon Initial Segment Plasticity and Excitability Homeostasis. *Neuron* **2019**, *104* (3), 458–470e5.
- (50) Combs, B.; Christensen, K. R.; Richards, C.; Kneynsberg, A.; Mueller, R. L.; Morris, S. L.; Morfini, G. A.; Brady, S. T.; Kanaan, N. M. Frontotemporal Lobar Dementia Mutant Tau Impairs Axonal Transport through a Protein Phosphatase  $\gamma$ -Dependent Mechanism. *J. Neurosci.* **2021**, *41* (45), 9431–9451.
- (51) Denk, F.; Wade-Martins, R. Knock-out and Transgenic Mouse Models of Tauopathies. *Neurobiol. Aging* **2009**, *30* (1), 1–13.
- (52) Frost, B.; Ollesch, J.; Wille, H.; Diamond, M. I. Conformational Diversity of Wild-Type Tau Fibrils Specified by Templated Conformation Change. *J. Biol. Chem.* **2009**, *284* (6), 3546–3551.
- (53) Chen, D.; Bali, S.; Singh, R.; Wosztal, A.; Mullanpudi, V.; Vaquer-Alicea, J.; Jayan, P.; Melhem, S.; Seelaar, H.; van Swieten, J. C.; Diamond, M. I.; Joachimiak, L. A. FTD-Tau S320F Mutation Stabilizes Local Structure and Allosterically Promotes Amyloid Motif-Dependent Aggregation. *Nat. Commun.* **2023**, *14* (1), No. 1625.
- (54) Sergeant, N.; Wattez, A.; Delacourte, A. Neurofibrillary Degeneration in Progressive Supranuclear Palsy and Corticobasal Degeneration: Tau Pathologies with Exclusively “Exon 10” Isoforms. *J. Neurochem.* **1999**, *72* (3), 1243–1249.
- (55) Umeda, Y.; Taniguchi, S.; Arima, K.; Piao, Y.-S.; Takahashi, H.; Iwatsubo, T.; Mann, D.; Hasegawa, M. Alterations in Human Tau Transcripts Correlate with Those of Neurofilament in Sporadic Tauopathies. *Neurosci. Lett.* **2004**, *359* (3), 151–154.
- (56) Barghorn, S.; Biernat, J.; Mandelkow, E. Purification of Recombinant Tau Protein and Preparation of Alzheimer-Paired Helical Filaments *In Vitro*. In *Amyloid Proteins*; Humana Press, 2005; Vol. 299, pp 35–51.
- (57) Aoyagi, H.; Hasegawa, M.; Tamaoka, A. Fibrillogenic Nuclei Composed of P301L Mutant Tau Induce Elongation of P301L Tau but Not Wild-Type Tau. *J. Biol. Chem.* **2007**, *282* (28), 20309–20318.
- (58) Chen, D.; Drombosky, K. W.; Hou, Z.; Sari, L.; Kashmer, O. M.; Ryder, B. D.; Perez, V. A.; Woodard, D. R.; Lin, M. M.; Diamond, M. I.; Joachimiak, L. A. Tau Local Structure Shields an Amyloid-Forming Motif and Controls Aggregation Propensity. *Nat. Commun.* **2019**, *10* (1), No. 2493.
- (59) Nacharaju, P.; Lewis, J.; Easson, C.; Yen, S.; Hackett, J.; Hutton, M.; Yen, S. H. Accelerated Filament Formation from Tau Protein with Specific FTDP-17 Missense Mutations. *FEBS Lett.* **1999**, *447* (2–3), 195–199.
- (60) Moreira, G. G.; Cristóvão, J. S.; Torres, V. M.; Carapeto, A. P.; Rodrigues, M. S.; Landrieu, I.; Cordeiro, C.; Gomes, C. M. Zinc Binding to Tau Influences Aggregation Kinetics and Oligomer Distribution. *Int. J. Mol. Sci.* **2019**, *20* (23), 5979.

- (61) Zhou, Z.; Fan, J.-B.; Zhu, H.-L.; Shewmaker, F.; Yan, X.; Chen, X.; Chen, J.; Xiao, G.-F.; Guo, L.; Liang, Y. Crowded Cell-like Environment Accelerates the Nucleation Step of Amyloidogenic Protein Misfolding. *J. Biol. Chem.* **2009**, *284* (44), 30148–30158.
- (62) Zhong, Q.; Congdon, E. E.; Nagaraja, H. N.; Kuret, J. Tau Isoform Composition Influences Rate and Extent of Filament Formation. *J. Biol. Chem.* **2012**, *287* (24), 20711–20719.
- (63) Meisl, G.; Kirkegaard, J. B.; Arosio, P.; Michaels, T. C. T.; Vendruscolo, M.; Dobson, C. M.; Linse, S.; Knowles, T. P. J. Molecular Mechanisms of Protein Aggregation from Global Fitting of Kinetic Models. *Nat. Protoc.* **2016**, *11* (2), 252–272.
- (64) Eves, B. J.; Douth, J. J.; Terry, A. E.; Yin, H.; Moulin, M.; Haertlein, M.; Forsyth, V. T.; Flagmeier, P.; Knowles, T. P. J.; Dias, D. M.; Lotze, G.; Seddon, A. M.; Squires, A. M. Elongation Rate and Average Length of Amyloid Fibrils in Solution Using Isotope-Labelled Small-Angle Neutron Scattering. *RSC Chem. Biol.* **2021**, *2* (4), 1232–1238.
- (65) Zhang, W.; Falcon, B.; Murzin, A. G.; Fan, J.; Crowther, R. A.; Goedert, M.; Scheres, S. H. Heparin-Induced Tau Filaments Are Polymorphic and Differ from Those in Alzheimer's and Pick's Diseases. *eLife* **2019**, *8*, No. e43584.
- (66) Chang, A.; Xiang, X.; Wang, J.; Lee, C.; Arakhamia, T.; Simjanoska, M.; Wang, C.; Carlomagno, Y.; Zhang, G.; Dhingra, S.; Thierry, M.; Perneel, J.; Heeman, B.; Forgrave, L. M.; DeTure, M.; DeMarco, M. L.; Cook, C. N.; Rademakers, R.; Dickson, D. W.; Petrucelli, L.; Stowell, M. H. B.; Mackenzie, I. R. A.; Fitzpatrick, A. W. P. Homotypic Fibrillization of TMEM106B across Diverse Neurodegenerative Diseases. *Cell* **2022**, *185* (8), 1346–1355e15.
- (67) Sumi, S. M.; Bird, T. D.; Nochlin, D.; Raskind, M. A. Familial Presenile Dementia with Psychosis Associated with Cortical Neurofibrillary Tangles and Degeneration of the Amygdala. *Neurology* **1992**, *42* (1), 120–127.
- (68) Poorkaj, P.; Bird, T. D.; Wijsman, E.; Nemens, E.; Garruto, R. M.; Anderson, L.; Andreadis, A.; Wiederholt, W. C.; Raskind, M.; Schellenberg, G. D. Tau Is a Candidate Gene for Chromosome 17 Frontotemporal Dementia. *Ann. Neurol.* **1998**, *43* (6), 815–825.
- (69) Rizzu, P.; Van Swieten, J. C.; Joosse, M.; Hasegawa, M.; Stevens, M.; Tibben, A.; Niermeijer, M. F.; Hillebrand, M.; Ravid, R.; Oostra, B. A.; Goedert, M.; van Duijn, C. M.; Heutink, P. High Prevalence of Mutations in the Microtubule-Associated Protein Tau in a Population Study of Frontotemporal Dementia in the Netherlands. *Am. J. Hum. Genet.* **1999**, *64* (2), 414–421.
- (70) Momeni, P.; Pittman, A.; Lashley, T.; Vandrovicova, J.; Malzer, E.; Luk, C.; Hulette, C.; Lees, A.; Revesz, T.; Hardy, J.; de Silva, R. Clinical and Pathological Features of an Alzheimer's Disease Patient with the MAPT Delta K280 Mutation. *Neurobiol. Aging* **2009**, *30* (3), 388–393.
- (71) Goedert, M.; Spillantini, M. G.; Jakes, R.; Rutherford, D.; Crowther, R. A. Multiple Isoforms of Human Microtubule-Associated Protein Tau: Sequences and Localization in Neurofibrillary Tangles of Alzheimer's Disease. *Neuron* **1989**, *3* (4), 519–526.
- (72) Montgomery, K. M.; Carroll, E. C.; Thwin, A. C.; Quddus, A. Y.; Hodges, P.; Southworth, D. R.; Gestwicki, J. E. Chemical Features of Polyanions Modulate Tau Aggregation and Conformational States. *J. Am. Chem. Soc.* **2023**, *145* (7), 3926–3936.
- (73) Lövestam, S.; Koh, F. A.; van Knippenberg, B.; Kotecha, A.; Murzin, A. G.; Goedert, M.; Scheres, S. H. W. Assembly of Recombinant Tau into Filaments Identical to Those of Alzheimer's Disease and Chronic Traumatic Encephalopathy. *eLife* **2022**, *11*, No. e76494.
- (74) Abskharon, R.; Sawaya, M. R.; Boyer, D. R.; Cao, Q.; Nguyen, B. A.; Cascio, D.; Eisenberg, D. S. Cryo-EM Structure of RNA-Induced Tau Fibrils Reveals a Small C-Terminal Core That May Nucleate Fibril Formation. *Proc. Natl. Acad. Sci. U.S.A.* **2022**, *119* (15), No. e2119952119.
- (75) Wesseling, H.; Mair, W.; Kumar, M.; Schlaffner, C. N.; Tang, S.; Beerepoot, P.; Fatou, B.; Guise, A. J.; Cheng, L.; Takeda, S.; Muntel, J.; Rotunno, M. S.; Dujardin, S.; Davies, P.; Kosik, K. S.; Miller, B. L.; Berretta, S.; Hedreen, J. C.; Grinberg, L. T.; Seeley, W. W.; Hyman, B. T.; Steen, H.; Steen, J. A. Tau PTM Profiles Identify Patient Heterogeneity and Stages of Alzheimer's Disease. *Cell* **2020**, *183* (6), 1699–1713e13.
- (76) Limorenko, G.; Lashuel, H. A. Revisiting the Grammar of Tau Aggregation and Pathology Formation: How New Insights from Brain Pathology Are Shaping How We Study and Target Tauopathies. *Chem. Soc. Rev.* **2022**, *51* (2), 513–565.
- (77) Alquezar, C.; Arya, S.; Kao, A. W. Tau Post-Translational Modifications: Dynamic Transformers of Tau Function, Degradation, and Aggregation. *Front. Neurol.* **2021**, *11*, No. 595532.
- (78) Necula, M.; Kuret, J. Pseudophosphorylation and Glycation of Tau Protein Enhance but Do Not Trigger Fibrillization in Vitro. *J. Biol. Chem.* **2004**, *279* (48), 49694–49703.
- (79) Despres, C.; Byrne, C.; Qi, H.; Cantrelle, F.-X.; Huvent, I.; Chambraud, B.; Baulieu, E.-E.; Jacquot, Y.; Landrieu, I.; Lippens, G.; Smet-Nocca, C. Identification of the Tau Phosphorylation Pattern That Drives Its Aggregation. *Proc. Natl. Acad. Sci. U.S.A.* **2017**, *114* (34), 9080–9085.
- (80) Liu, F.; Li, B.; Tung, E.-J.; Grundke-Iqbal, I.; Iqbal, K.; Gong, C.-X. Site-Specific Effects of Tau Phosphorylation on Its Microtubule Assembly Activity and Self-Aggregation: Site-Specific Effects of Tau Phosphorylation. *Eur. J. Neurosci.* **2007**, *26* (12), 3429–3436.
- (81) Cohen, T. J.; Guo, J. L.; Hurtado, D. E.; Kwong, L. K.; Mills, I. P.; Trojanowski, J. Q.; Lee, V. M. Y. The Acetylation of Tau Inhibits Its Function and Promotes Pathological Tau Aggregation. *Nat. Commun.* **2011**, *2* (1), No. 252.
- (82) Moore, C. L.; Huang, M. H.; Robbennolt, S. A.; Voss, K. R.; Combs, B.; Gamblin, T. C.; Goux, W. J. Secondary Nucleating Sequences Affect Kinetics and Thermodynamics of Tau Aggregation. *Biochemistry* **2011**, *50* (50), 10876–10886.
- (83) Winsor, C. P. The Gompertz Curve as a Growth Curve. *Proc. Natl. Acad. Sci. U.S.A.* **1932**, *18* (1), 1–8.
- (84) Kang, S.-G.; Han, Z. Z.; Daude, N.; McNamara, E.; Wohlgemuth, S.; Molina-Porcel, L.; Safar, J. G.; Mok, S.-A.; Westaway, D. Pathologic Tau Conformer Ensembles Induce Dynamic, Liquid-Liquid Phase Separation Events at the Nuclear Envelope. *BMC Biol.* **2021**, *19* (1), No. 199.
- (85) Espinoza, M.; de Silva, R.; Dickson, D. W.; Davies, P. Differential Incorporation of Tau Isoforms in Alzheimer's Disease. *J. Alzheimers Dis.* **2008**, *14* (1), 1–16.
- (86) Anderberg, M. R. *Cluster Analysis for Applications*; Academic Press/Elsevier Science: Burlington, 2014.
- (87) Pedregosa, F.; Varoquaux, G.; Gramfort, A.; Michel, V.; Thirion, B.; Grisel, O.; Blondel, M.; Prettenhofer, P.; Weiss, R.; Dubourg, V.; Vanderplas, J.; Passos, A.; Cournapeau, D.; Brucher, M.; Perrot, M.; Duchesnay, E. Scikit-Learn: Machine Learning in Python. *J. Mach. Learn. Res.* **2011**, *12* (85), 2825–2830.
- (88) Virtanen, P.; Gommers, R.; Oliphant, T. E.; Haberland, M.; Reddy, T.; Cournapeau, D.; Burovski, E.; Peterson, P.; Weckesser, W.; Bright, J.; van der Walt, S. J.; Brett, M.; Wilson, J.; Millman, K. J.; Mayorov, N.; Nelson, A. R. J.; Jones, E.; Kern, R.; Larson, E.; Carey, C. J.; Polat, İ.; Feng, Y.; Moore, E. W.; VanderPlas, J.; Laxalde, D.; Perktold, J.; Cimrman, R.; Henriksen, I.; Quintero, E. A.; Harris, C. R.; Archibald, A. M.; Ribeiro, A. H.; Pedregosa, F.; van Mulbregt, P.; SciPy 1.0 Contributors; et al. SciPy 1.0: Fundamental Algorithms for Scientific Computing in Python. *Nat. Methods* **2020**, *17* (3), 261–272.